High-throughput and Data-Driven Search for Stable Optoelectronic AMSe3 Materials

Journal:	*Journal of Materials Chemistry A*
Manuscript ID	TA-ART-12-2024-008867.R1
Article Type:	Paper
Date Submitted by the Author:	29-Jan-2025
Complete List of Authors:	Singh, Nikhil; Indian Institute of Technology Delhi, Department of Chemistry Samanta, Kushal; IIT Delhi, Dept. Materials Science and Engg. Maharana, Suneet K.; Indian Institute of Technology Kanpur, Department of Chemistry Pal, Koushik; Northwestern University, Materials Science and Engineering Tretiak, Sergei; Los Alamos National Laboratory, Theoretical Division Talapatra, Anjana; LANL Ghosh, Dibyajyoti; IIT Delhi,

High-throughput and Data-Driven Search for Stable Optoelectronic $AMSe_3$ Materials

Nikhil Singh,[1, #] Kushal Samanta,[2, #] Suneet K. Maharana,[3] Koushik Pal[4], Sergei Tretiak[5], Anjana Talapatra[6], Dibyajyoti Ghosh[1,2*]

[1]*Department of Chemistry, Indian Institute of Technology, Delhi, Hauz Khas, New Delhi 110016, India*

[2]*Department of Materials Science and Engineering, Indian Institute of Technology, Delhi, Hauz Khas, New Delhi 110016, India*

[3]*Department of Chemistry, Indian Institute of Technology Kanpur, Kanpur, UP 208016, India*

[4]*Department of Physics, Indian Institute of Technology Kanpur, Kanpur 208016, India*

[5]*Theoretical Division and Center for Integrated Nanotechnologies, Los Alamos National Laboratory, Los Alamos, New Mexico 87545, United States*

[6]*Materials Science and Technology Division, Los Alamos National Laboratory, Los Alamos, NM, 87544, USA*

#: These authors contributed equally

Abstract:

The rapid advancement in emerging optoelectronic technologies demand highly efficient, affordable, and ecofriendly materials. In this context, ternary chalcogenides especially ternary selenides show early promise as a material class due to their stability and remarkable electronic, optical, and transport properties. Here, we integrate first-principles-based high-throughput computations with machine learning (ML) techniques to predict the thermodynamic stability and optoelectronic properties of 920 valency-satisfied selenide compounds. Through investigating polymorphism, our study reveals the edge-sharing orthorhombic *Pnma* phase (NH_4CdCl_3-type) as the most stable structure for most ternary selenides. High fidelity supervised ML models are trained and tested to accelerate stability and band gap predictions. These data-driven models pin down the most influential features that dominantly control key material characteristics. The multistep high-throughput computations identify the ternary selenides with optimal direct band gaps, light carrier masses, and strong optical absorption edges. The extensive materials screening considering phase stability, toxicity, and defect tolerance, finally identifies the seven most suitable candidates for photovoltaic applications. Two of these final compounds, $SrZrSe_3$ and $SrHfSe_3$, have already been synthesized in single-phase form, with the latter showing an optically suitable band gap, aligning well with our findings. The non-adiabatic molecular dynamics reveal sufficiently long photoexcited charge carrier lifetimes (on the order of nanoseconds) in some of these selected selenide materials, indicating their exciting characteristics. Overall, our study suggests a robust *in-silico* framework that can be extended to screen large datasets of various material classes for identifying promising photoactive candidates.

Introduction

Efficient optoelectronic technologies, such as solar cells and light-emitting devices (LEDs), are emerging as one of the most promising responses to the pressing global energy crisis and the environmental impact of fossil fuel dependence. Over the past few decades, various optoelectronic materials have been discovered and extensively optimized for highly efficient device performance.[1–4] Prominent examples include silicon and CdTe,[5–7] extensively used in solar photovoltaic technologies, and traditional III-V semiconductors commonly used in LEDs.[8,9] While silicon-based photovoltaics currently dominate the global market, ongoing efforts focus on identifying alternative cost-effective semiconductors with superior performances.[10–15] Metal halide perovskites have garnered considerable interest in the last decade as viable options for solar applications owing to their outstanding optoelectronic features and cost-efficient production process.[16,17] However, the intrinsic instability under environmental conditions and the ubiquitous presence of toxic Pb adversely impact their commercialization.[18] Recently, toxic-element-free ternary chalcogenides have attracted considerable research interest due to their excellent optoelectronic properties and superior structural stability under ambient conditions.[19,20] The general chemical formula of these compounds is AMX_3, where A and M are cations with a range of oxidation states ranging from +1 to +5, and X is a chalcogen, either S or Se. The possibility of accommodating A and M with several oxidation state pairs provide an opportunity to enumerate large chemical space, finding the most suitable chalcogenides for targeted applications.

The predominant covalent character of chalcogenides frequently gives rise to their narrow band gaps, which are beneficial for efficient solar energy harvesting for photovoltaics and photocatalysis.[21] Furthermore, the AMX_3 compounds exhibit a unique bonding nature due to the moderate electronegativity of S and Se, which are less electronegative than oxygen and halogens but more so than non-metal elements like Si and Ge. Sun *et al.* employed density functional theory (DFT) to find suitable optoelectronic properties of several chalcogenides, while exploring the perovskites phase of AMX_3 (A = Ca, Sr, Ba; M = Ti, Zr, Hf; X = S, Se).[22] Extensive high-throughput computational screening of ternary sulfides (AMS_3) by Kuhar et al. identified candidates with suitable electronic and optical properties for photoactivity. Their study reported the synthesis and characterization of $LaYS_3$ thin film that shows a direct band gap of 2 eV.[23] Zhang et al. computationally found and experimentally verified that the perovskite phase of $LaScSe_3$ is thermodynamically stable with a slightly wider band gap of ~2.2 eV.[24] Driven by their emerging attractive photoactivity, several ternary chalcogenides are now being synthesized as single crystals, thin films, and colloidal nanocrystals.[21] In addition to traditional high-temperature solid-state reactions, approaches like magnetron sputtering,[25] pulse laser deposition,[26] molecular beam epitaxy,[27] and chemical solution deposition[28] are gaining popularity in synthesizing high-quality chalcogenides at relatively mild experimental conditions. Regarding direct characterization, Niu et al. found comparable and better external and internal luminescence efficiency of $SrZrS_3$ than traditional semiconductors, suggesting their potential optoelectronic applications. The minimal shift in the photoluminescence peak of $LaYS_3$ thin film indicates its attractive photoactivity. [29] Moroz et al. employed the optical diffuse reflectance measurements to find a band gap of ~1 eV for $SrHfSe_3$ that has been synthesized through a high-temperature solid-state reaction.[30].

Despite these recent remarkable advancements[14,15,20–22,26–28,31–36], ternary chalcogenides, especially selenides remain largely underexplored. Their pronounced polymorphism, which is an ability to form different structural phases of the same AMX_3 compound, raises a critical challenge for their long-term phase stability. It is worth mentioning that most of the reports so far focused on the corner-sharing orthorhombic perovskite phase of sulfides as it closely resembles halide perovskites.[22,23,31] However, this geometry often appears thermodynamically unstable or metastable compared to other non-perovskite phases, indicating limited stability under ambient conditions. A comprehensive computational study, encompassing the entire chemical space and accounting for other stable perovskite/non-perovskite phases, is essential to tap into the potential of these ternary chalcogenides for optoelectronic applications.

In this work, we integrate several atomistic simulation techniques such as DFT, *ab initio* molecular dynamics (AIMD), non-adiabatic molecular dynamics (NAMD) and Machine Learning (ML) based models to identify promising ternary selenide $AMSe_3$ compounds for photovoltaics and other applications. While AMS_3 compounds have been extensively studied using high-throughput approaches,[37] $AMSe_3$ systems remain relatively underexplored despite their frequent demonstration of thermodynamic stability and promising optoelectronic properties. On the other hand, $AMTe_3$ compounds, although intriguing, often exhibit poor structural stability and have never been reported experimentally, which diminishes their practical relevance and makes them less attractive for computational studies.[38] The available chemical space and valency consideration provide an initial dataset of 920 distinct combinations of $AMSe_3$. Rigorous phase stability analysis of randomly selected candidates identifies the most commonly realized ground-state structure. The extensive *in-silico* study of thermodynamic stability and band gap analyses substantially narrowed down the list of potential materials for optoelectronic applications. The complete dataset has been provided as separate file. We train and test high-accuracy ML models to predict formation energy, Hull stability, and electronic band gaps for $AMSe_3$ compounds. Subsequent multi-stage materials filtering considering crucial properties such as direct band gap, low carrier effective masses, eco-friendliness, and defect tolerance, yields a list of the most suitable ternary selenides for optoelectronics. Finally, NAMD simulations reveal extended excited carrier lifetimes in three of these $AMSe_3$, indicating their superior properties. The identification of already synthesized $SrHfSe_3$ and $SrZrSe_3$ in the final list of potential candidates suggests the feasibility of experimentally realizing other screened compounds.

Results:

Ternary selenide chemical space: Our primary focus is to explore the entire chemical space of ternary selenide materials $AMSe_3$, by varying atomic species A and M throughout the periodic table. The exclusion of inert gases, lanthanides (except La), actinides, and post-actinides results in $54 \times 53 = 2862$ possible ternary selenide compounds, excluding two-component A_2Se_3 or B_2Se_3

species (Supplemental Figure S1). Additionally, we confine ourselves to A-M combinations that maintain overall charge neutrality of $AMSe_3$. Thus, A and M can have following pair of oxidation states (+1, +5) (+2, +4) (+3, +3) (+4, +2) and (+5, +1), ensuring that the sum of the valences of cations and anions vanishes. These criteria yield 920 ternaries in total open for further investigation (Supplemental Figure S1). Note that any pair of suitable elements X and Y define distinct $XYSe_3$ and $YXSe_3$ structures in our dataset due to non-equivalent Wyckoff positions of A and M sites and their dissimilar oxidation states and ionic radii.

Phase Stability

Ternary chalcogenides feature polymorphism where each structural type exhibits distinct bonding pattern.[21] With 920 materials, the challenge lies in identifying the most stable phase for each $AMSe_3$ composition using conventional crystal structure prediction approaches like CALYPSO[39] and USPEX.[40] Thus, we search for the most stable structure using the prototype structures approach as employed previously.[37,41] The available experimental structures depict that AMX_3 (X = S, Se) compounds mostly crystalize in a few distinct phases: (i) $GdFeO_3$-type orthorhombic *Pnma* structure, a perovskite with corner-sharing octahedra, (ii) NH_4CdCl_3-type orthorhombic *Pnma* structure, a non-perovskite with edge-sharing octahedra (needle-like phase), (iii) $FePS_3$-type monoclinic C12/m1 structure, a layered non-perovskite with edge-sharing octahedra, (iv) $PbPS_3$-type monoclinic P1c1 structure with no octahedral. Figure 1(a-d) displays these representative structures. To assess the relative phase stability of $AMSe_3$, we compute the total energy (see Methods section) of a subset of 200 randomly chosen compounds, which are optimized in these four different phases (Supplemental Table S1).

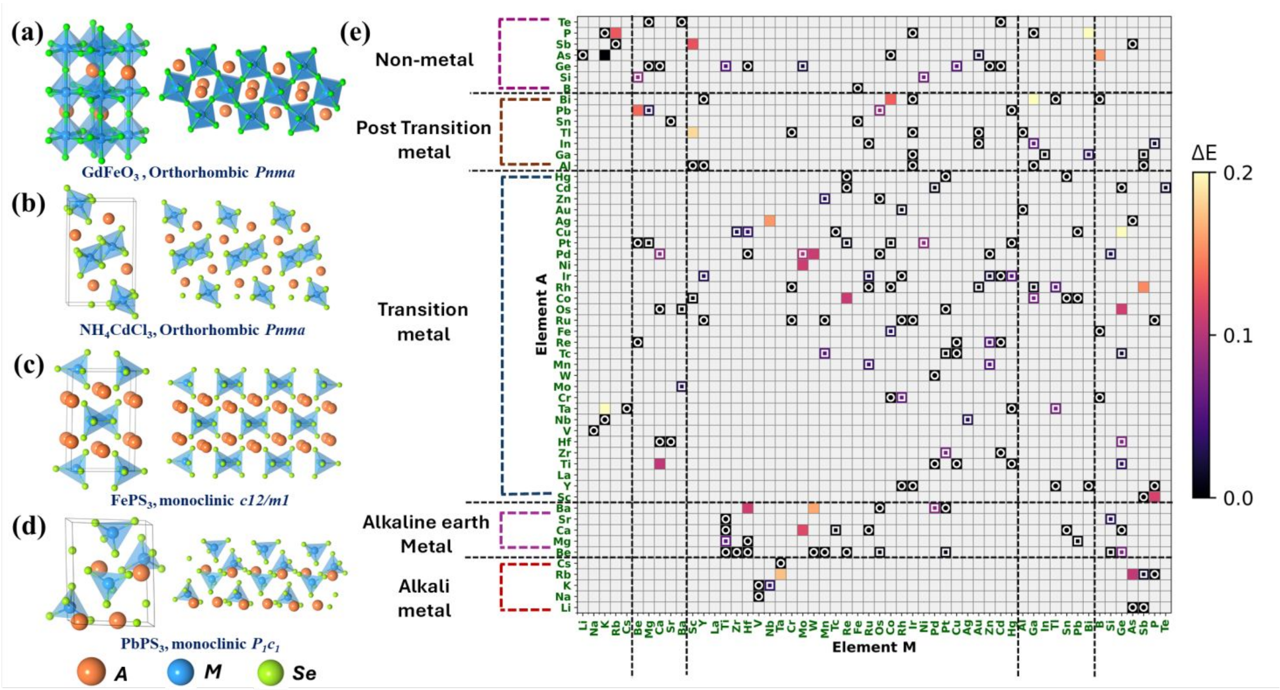

Figure 1. *Representative structures of (a) $GdFeO_3$, (b) NH_4CdCl_3, (c) $FePS_3$, (d) $PbPS_3$-type phases of $AMSe_3$ compounds. (e) Phase stability investigation of 200 randomly selected $AMSe_3$. The heatmap depicts the calculated energy difference (ΔE) between the NH_4CdCl_3-type orthorhombic phase and the most stable phase. Special markers: White circles represent compounds with $\Delta E=0$ (stable in NH_4CdCl_3-type orthorhombic phase), white hollow squares represent compounds with $0<\Delta E<0.1$ eV (metastable in NH4CdCl3-type orthorhombic phase). Here ΔE is defined as the difference between the NH_4CdCl_3-type orthorhombic phase and the most stable phase energies.*

Computed total energies of $AMSe_3$ in various crystal structure motifs reveal that NH_4CdCl_3-type orthorhombic phase is most frequently stable (56.5%), followed by $PbPS_3$-like monoclinic P1c1 (20.5%), $FePS_3$-like monoclinic C12/m1 (14.5%), and $GdFeO_3$-like orthorhombic Pnma structure (8.5%), see Figure 1e. Furthermore, 32% of $ABSe_3$ compounds that are less stable in the NH_4CdCl_3-type structure, are found to be metastable, within 0.1 eV/atom of the ground-state geometry. Thus, 88.5% of selected $AMSe_3$ are either mostly stable or marginally metastable in the orthorhombic non-perovskite phase. Previous studies have also identified NH_4CdCl_3-type structure of $AMSe_3$ as the most stable phase (Supplemental Section S2.1).[33,35] The frequent phase stability of edge-sharing polyhedra-containing structures demonstrates that ternary selenides do not obey Pauling's third rule.[42] We note that dominant covalent bonding and subsequent weak Coulomb repulsion between B-site cations of in adjacent polyhedral facilitate the stabilization of the NH_4CdCl_3-type phase. Given these observations, we next structurally optimize and explore the remaining $AMSe_3$ candidates (720 out of 920), focusing exclusively on the NH_4CdCl_3-type orthorhombic phase.

Crystal Structure of NH_4CdCl_3-like orthorhombic phase: Figure 1b and Supplemental Figure S2 show a prototype of $AMSe_3$ in the NH_4CdCl_3-like orthorhombic phase. The edge-sharing MSe_6 octahedra, which form 1D chains along the x-axis, remain stacked through electrostatic interactions between A cations and Se anions along the other axes (y and z). Thus, these $AMSe_3$ compounds exhibit inherent structural anisotropy due to their dissimilar crystal packing along different crystal directions. The distribution of lattice constants for the entire dataset suggests that the 'a' parameter varies significantly less than the 'b' and 'c' parameters (Supplemental Figure S3). The 1D-chains of MSe_6 edge-sharing octahedra leads to a limited variation along the a-axis. In contrast, the less dense stacking of octahedra along the 'b' and 'c' axes with more intervening space, results in broader fluctuations across the chemical space. More detailed discussions are included in Supplemental Section S2.2.

Thermodynamic stability

In-silico assessment of thermodynamic stability is a key step for accelerated materials screening and selection.[43,44] To identify stable $AMSe_3$ compounds from the dataset, we compute two well-established properties, namely formation energy (E_f) and hull distance (E_h). Among these, E_f is a relatively relaxed criterion compared to E_h for screening stable compounds (Supplemental Section S3.1). Thus, E_f is initially used to segregate $AMSe_3$ into two distinct categories: formable ($E_f \leq 0$ eV/atom) and non-formable ($E_f > 0$ eV/atom). We find that 93% of $AMSe_3$ compounds are formable, which implies the frequent stability of ternary selenides relative to their elemental standard states of A, M, and Se (Figure 2 and Supplemental Figure S4a). These formable compounds are further split into three groups based on hull distance (E_h): phase stable with $E_h \leq 0.1$ eV/atom, metastable with $0.1 < E_h \leq 0.2$ eV/atom, and unstable with $E_h > 0.2$ eV/atom (Figure 2 and Supplemental Figure S4c). This classification reveals that 24%, 36%, and 33% of $AMSe_3$ candidates are hull stable, metastable, and unstable, respectively (Supplemental Figure S4c). Thus, about one-third of ternary selenides that are stable against their constituent elemental phases, can decompose into relatively more stable binary or ternary phases. This underpins the importance of computing E_h alongside E_f for reliable predictions of material stability, as these two quantities do not exhibit any noticeable correlation (Supplemental Figure S4d). Our study identifies 25 $AMSe_3$ candidates with $E_h = 0$ eV/atom, depicting their stability against competing structural phase(s) and all possible decomposed constituting phases (Figure 2 and Supplemental Table S2).

Traditionally, materials with $E_h > 0$ eV/atom have been considered synthetically challenging and prone to long-term stability due to spontaneous decomposition into other phases.[45] However, advancements in solid-state synthesis procedures, including improved control over experimental conditions, have made possible to realize metastable materials in their stable form.[46–49] Moreover, the present stability data are computed at 0 K, without considering the entropy contribution to the free energy at finite temperatures. Such an entropy factor can potentially further stabilize the selenide compounds with marginally positive hull stability. Therefore, using relaxed criteria for thermodynamic stability, $E_h \leq 0.1$ eV/atom, allow us to identify metastable yet functionally promising $AMSe_3$ compounds during *in-silico* screening. Supplemental Section S3.2 provides a brief discussion of the recent progress in synthesizing metastable phases of materials.

The thermodynamic stability maps in Figure 2 and Supplemental Figure S5 further categorize the entire chemical space according to common elemental groups. The map reveals that most $AMSe_3$ compounds with alkaline earth metals as M exhibit high formability but poor hull stability. In contrast, post-transition metals/non-metals as A and transition metals/post-transition metals as M emerge with much more frequent phase stability. The $AMSe_{3,}$ compounds with transition metals in both A and M positions exhibit relatively lower stability (Supplemental Figure S5). Overall, we do not find strong trends in chemical stability regions for these compounds, underscoring their complex relation between stability and composition.

Commonly used radius ratios, such as the Goldschmidt tolerance factor, octahedral factor, and modified tolerance factor, are effective for classifying stability regions for perovskite and non-perovskite phases.[50,51] However, those metrics perform poorly in identifying the stability range for NH_4CdCl_3-type orthorhombic phases of $AMSe_3$ (Supplemental Figure S6). This fundamental limitation is attributed to the prevailing covalent character of M-Se bonds, which contrasts with the predominantly ionic bonding typically found in oxides and halides for which these geometric factors were formulated.[52] The intricate chemical bonding prompts moving beyond simple geometric descriptors and develop more robust ML models for accurately predicting the thermodynamic stability of these ternary selenides.

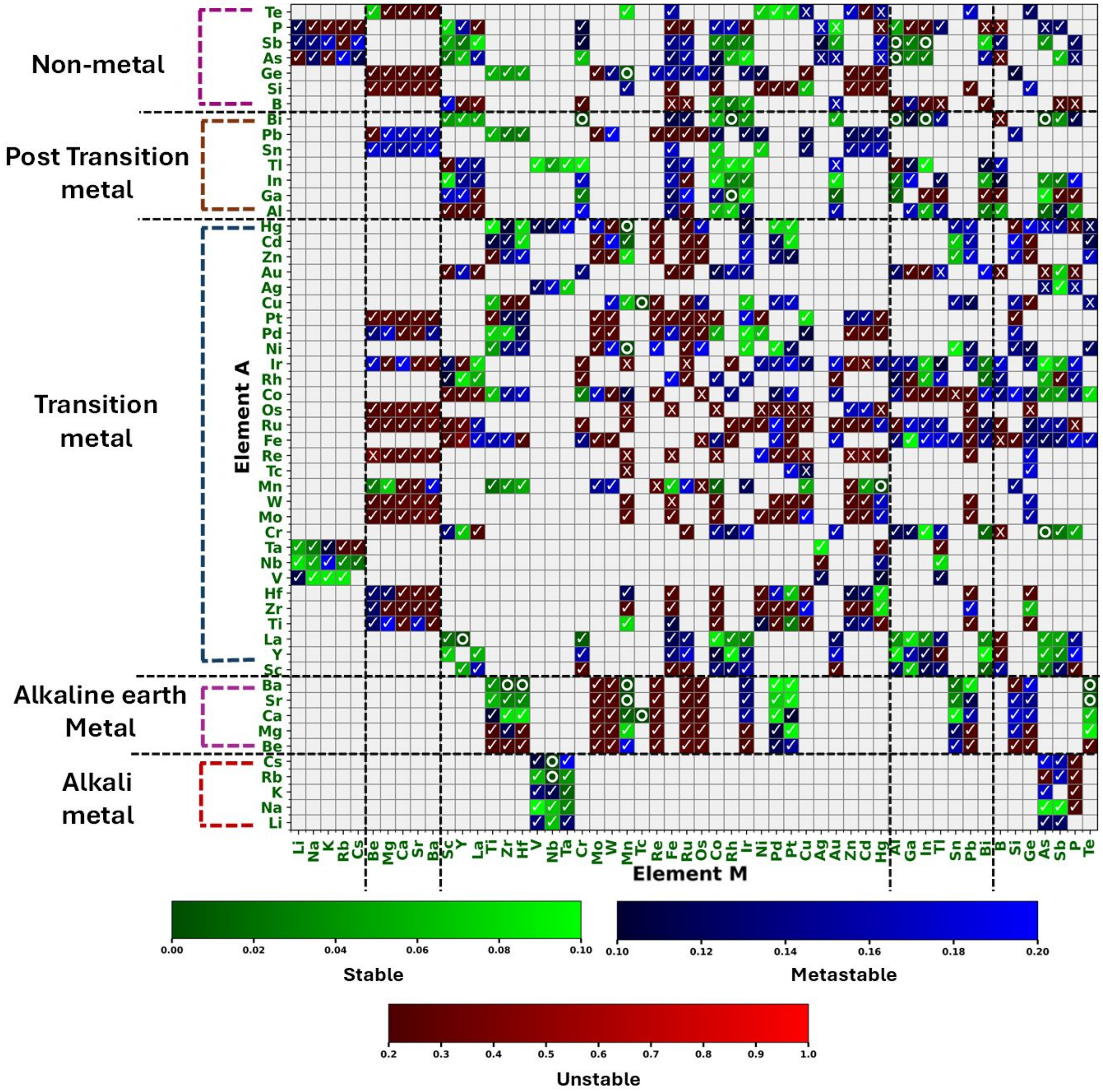

Figure 2. *A composition map of A/M elements depicting energy above hull (E_h) values across the entire chemical space. White rings denote highly stable compositions with $E_h \leq 0.01$ eV/atom and $E_f \leq 0$ eV/atom. Crosses (×) represent $AMSe_3$ compounds with $E_f > 0$ eV/atom. Boxes marked with a 'tick' indicate compounds with $E_f \leq 0$/atom and $E_h > 0.01$ eV. The gradient color bars highlight different stability classes of $AMSe_3$.*

ML model for stability: We next train and test supervised ML models that can quantitatively predict the formation energies and hull stability for the complete AMSe$_3$ dataset. These models use relevant data calculated using computationally affordable semi-local PBE-GGA functional. Two types of initial ML models are developed: (1) models based solely on elemental and compositional features, and (2) models including lattice parameters of the crystal as additional features.

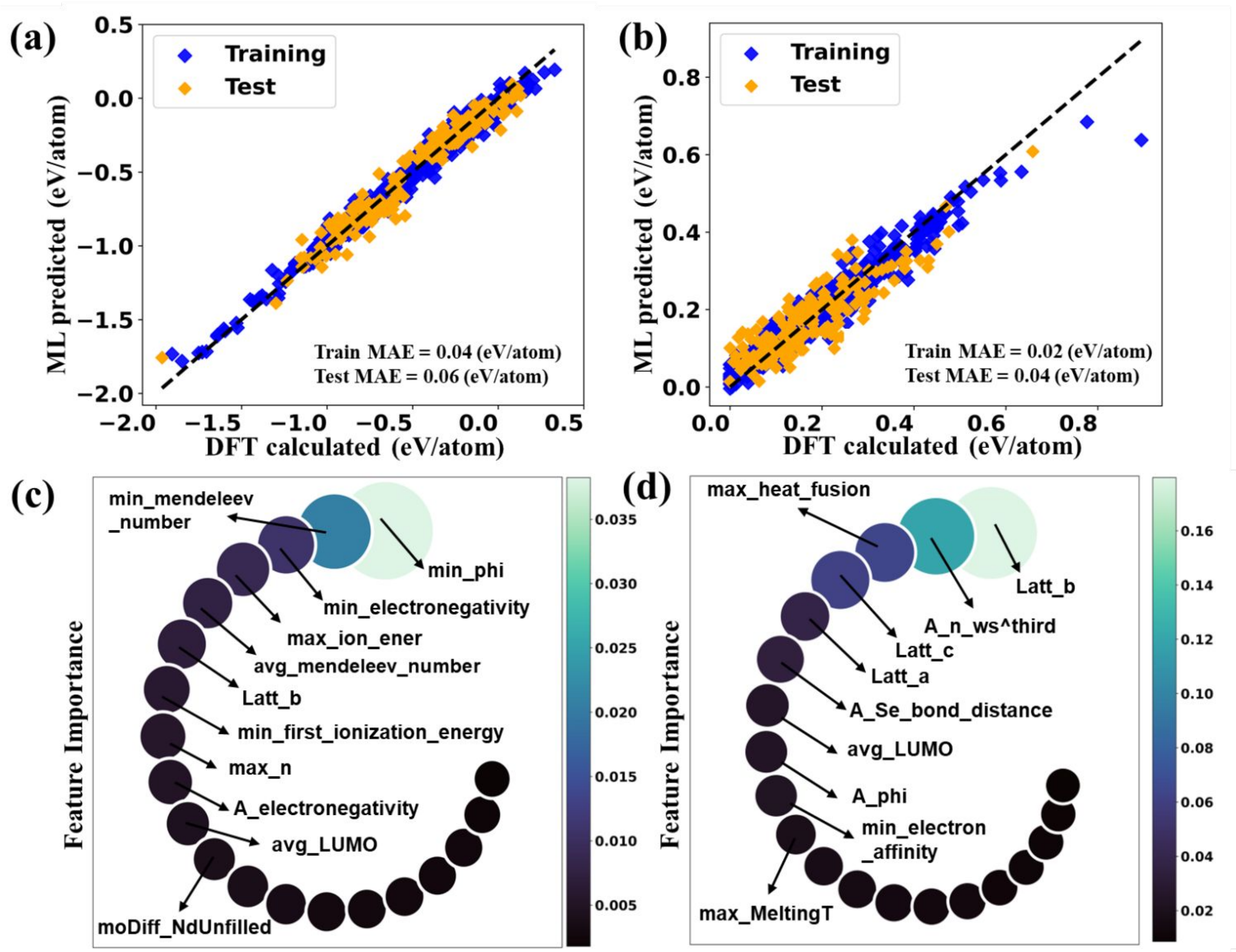

Figure 3. *The supervised regression models for structural stability are illustrated with parity plots: (a) formation energy predictions using the gradient boosting regressor model, and (b) hull*

distance predictions using the histogram-based (hist) gradient boosting regressor model. These ML models include lattice parameters as features to improve prediction accuracy. The feature importance ranking for these formation energy and hull stability prediction models are shown in panels (c) and (d), respectively.

***Formation energy**:* First, we trained and tested regression models for E_f using various elemental and compositional features. We selected gradient-boosting algorithms due to their proven effectiveness in handling complex, nonlinear relationships in materials science datasets. These ensemble methods combine multiple weak learners (typically decision trees) to form a strong predictive model, which is particularly suitable for capturing intricate patterns in formation energy data. Among these models, the gradient boosting regressor[53] achieves the best prediction accuracy with an MAE of 0.067 eV/atom for the test set (Supplemental Figure S7a). Other models, including histogram-based (hist) gradient boosting regressor[54] and extreme gradient boosting regressor,[55] also efficiently predicts E_f for ternary selenides (Supplemental Figure S7b). These specific ML models are robust against overfitting and handle mixed data types as shown in previous materials property predictions.[55,56]

In the next step, the regression models are trained with lattice parameters (a, b, and c) as features. Previous studies have highlighted the necessity of incorporating structural information to construct reliable ML models for material stability predictions.[57] However, these structural parameters are only available once the ground-state geometry is known, which limits the applicability of trained ML models for predicting stability in entirely new compositions. To minimize the dependence on structural information, we train ML models using only the lattice parameters as features. Among the tested models, the gradient boosting regressor achieves the highest accuracy for predicting E_f with a test MAE of 0.06 eV/atom (Figure 3a). The E_f prediction errors are comparable to or even better than those of previously reported models.[58–60] Thus, our results indicate that incorporating structural parameters as features reduces the MAE and improves the prediction accuracy of E_f by approximately 11%.

Hull stability: As hull stability (E_h) depends on the energetics of competing compounds, its accurate prediction through ML models is more challenging than evaluation of E_f.[57,61] Our study illustrates that including lattice parameters along with compositional and elemental features is essential for a reliable prediction of E_h (Supplemental Section S4.1). The hist gradient boosting regressor model achieves the best performance among all tested models, with a test MAE of only 0.04 eV/atom when lattice parameters are included as features. The performance of other models and the impact of including structural information in ML models are further discussed in Supplemental Section S4.1.

Here we note that the ML models including E_f and excluding lattice parameters as features exhibit similar predictive performance for E_h (Supplemental Figure S8). Thus, despite poor direct correlations between E_f and E_h (see Supplemental Figure S4(d)), the ML models reveal the crucial role of E_f values in predicting E_h of $AMSe_3$ compounds. These findings further suggest that access to high-fidelity E_f data is sufficient for predicting E_h without structure information for $ABSe_3$.

Feature importance of best performing ML model: We conduct feature importance analyses using permutation feature importance, a model-agnostic technique, for the best-performing regression models (Supplemental Section S4.2). As depicted in Figure 3c, elemental features such as the minimum value of work function (min_phi), electronegativity (min_Electronegativity), Mendeleev number (min_MendeleevNumber), are the most influential features for E_f prediction. Structural features, such as lattice parameter ‘b’, also appear in the top ten most important features, however, their significance is notably lower than that of the top ones. The relatively weaker importance of structural features justifies the marginal improvement in the model performance when they are incorporated during training. In contrast, the lattice constants emerge as highly important features in predicting E_h, where all three parameters appear in the top five on the feature list (Figure 3d). The high importance of lattice parameters aligns with the much-improved model accuracy of machine-learned E_h predictions, when these features are included in training and testing. Note that other models exhibit similar or worse accuracy in predicting E_h and similar stability indicators without structural input while considering much larger datasets.[51,57,62]

Material screening based on stability**:** The high-throughput material screening of $AMSe_3$ employs thermodynamic stability criteria of $E_f < 0$ eV/atom and $\Delta E_h < 0.1$ eV/atom. These relatively strict criteria separate ternary selenides that are stable and most likely do not need special synthesis approaches. Out of the initial 920 $AMSe_3$ candidates, only 222 appear structurally stable (Figure 2). Consequently, 76% of selenides in the entire dataset are discarded, underscoring the importance of computing thermodynamic stability early in the high-throughput materials screening protocol.

A careful check reveals that the screened stable candidates include most of the $AMSe_3$ compounds previously reported in the literature. Notably, hull stable candidates $SrHfSe_3$ and $SrZrSe_3$ have been synthesized in the NH_4CdCl_3-type orthorhombic phase.[30,63] Ong et al. employed evolutionary methods to find the ground state structure of $BaZrSe_3$ in the same phase.[64] Moreover, Adhikari *et al.* and Sun et al. explored the phase stability of a few $AMSe_3$ (A = Ca, Sr, Ba; M = Zr, Hf), with most of the compounds computationally predicted to be stable in NH_4CdCl_3-type phase.[35]

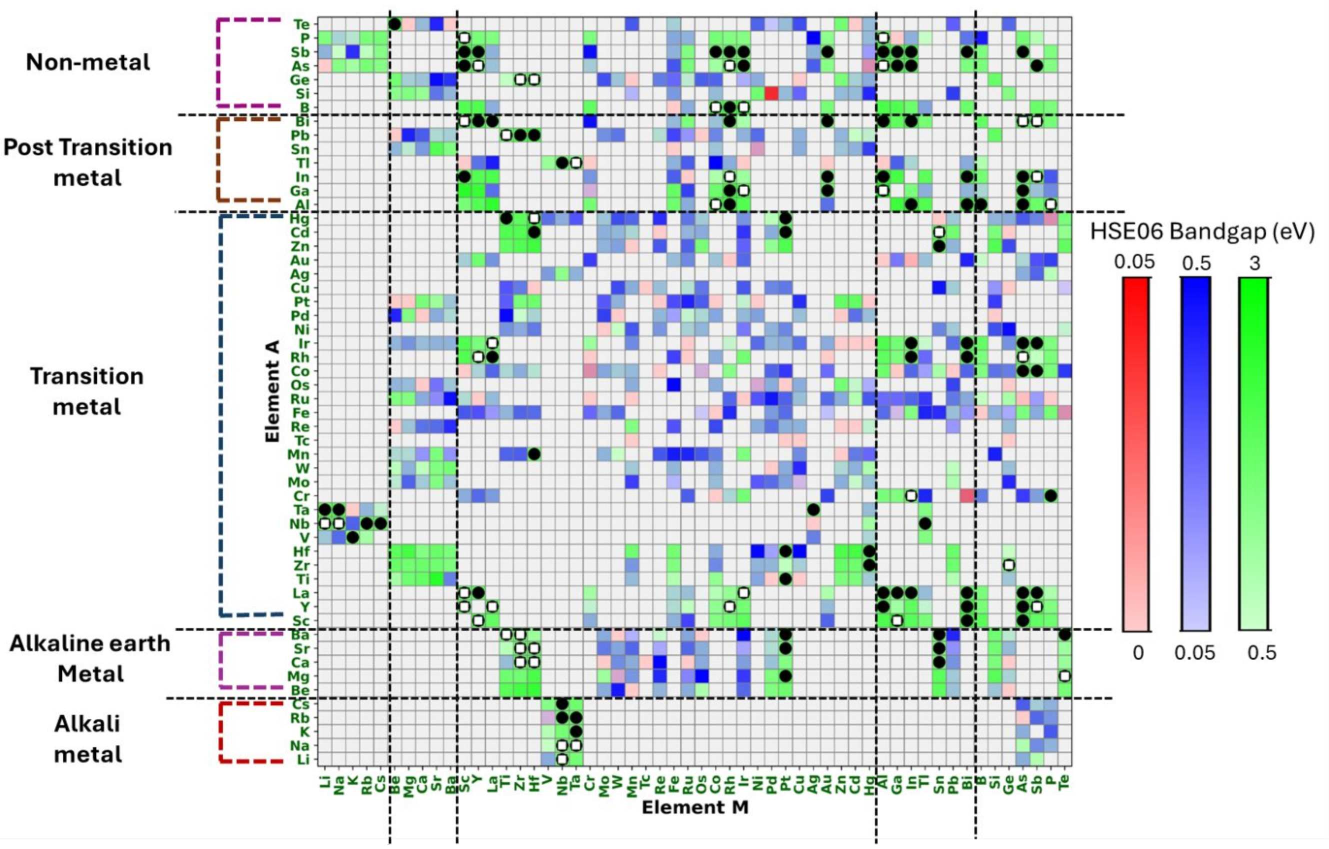

Figure 4: *The elemental map displays the band gap data obtained with the HSE06 functional for all 920 $AMSe_3$ compounds. The band gap values are represented by three different colored bars as shown in the right. Black circles highlight compounds with $E_h < 0.1$ eV and HSE06 bandgap > 0.5 eV, while white squares overlaid on black circles denote $AMSe_3$ compounds with direct band gaps.*

Electronic Properties:

The photovoltaic efficiency of absorber semiconductors intimately depends on their band gap values, as described by the Shockley-Queisser limit.[65] Therefore, finding optimal band gap systems through DFT-based high-throughput screening and, more recently, ML-based models, has emerged as the elementary step for *in-silico* design of optoelectronic material. To develop a reliable ML model for band gap (E_g) prediction, we compute the electronic structures of $AMSe_3$ using semi-local GGA-PBE functional and the more accurate hybrid HSE06 functional, regardless of their thermodynamic stability.

Band Gap distribution: Figure 4 shows the calculated HSE06 band gap values for all 920 $AMSe_3$ candidates. There are ~ 37% of the candidates (339 systems) with band gap values of $E_g \leq 0.05$ eV that are not suitable for optoelectronic applications. These $AMSe_3$ mostly populate the chemical space where both A and M are transition metals (Figure 4). The $AMSe_3$ candidates with $E_g > 0.5$ eV are ~34% of the total dataset (315 systems) and are potentially relevant for photovoltaics. These ternary selenides predominantly emerge from the chemical space where A and M are nonmetals.

We next examine the relationship between material stability and electronic band gap in these ternary selenides. Figure 5a illustrates that 82% (258 systems) of wide band gap $AMSe_3$ (with $E_g > 0.5$ eV) are stable or metastable ($E_f \leq 0$ eV/atom and $E_h \leq 0.2$ eV/atom). In contrast, only 25% of metastable and unstable $AMSe_3$ appear as wide band gap candidates, illustrating their prevalent metallic/narrow band gap characteristics (Figure 5a). Our data-driven analysis suggests potential labor-intensive experimental efforts required to stabilize these materials through synthetic optimization process if low-gap compounds from this family are needed for optoelectronic applications.

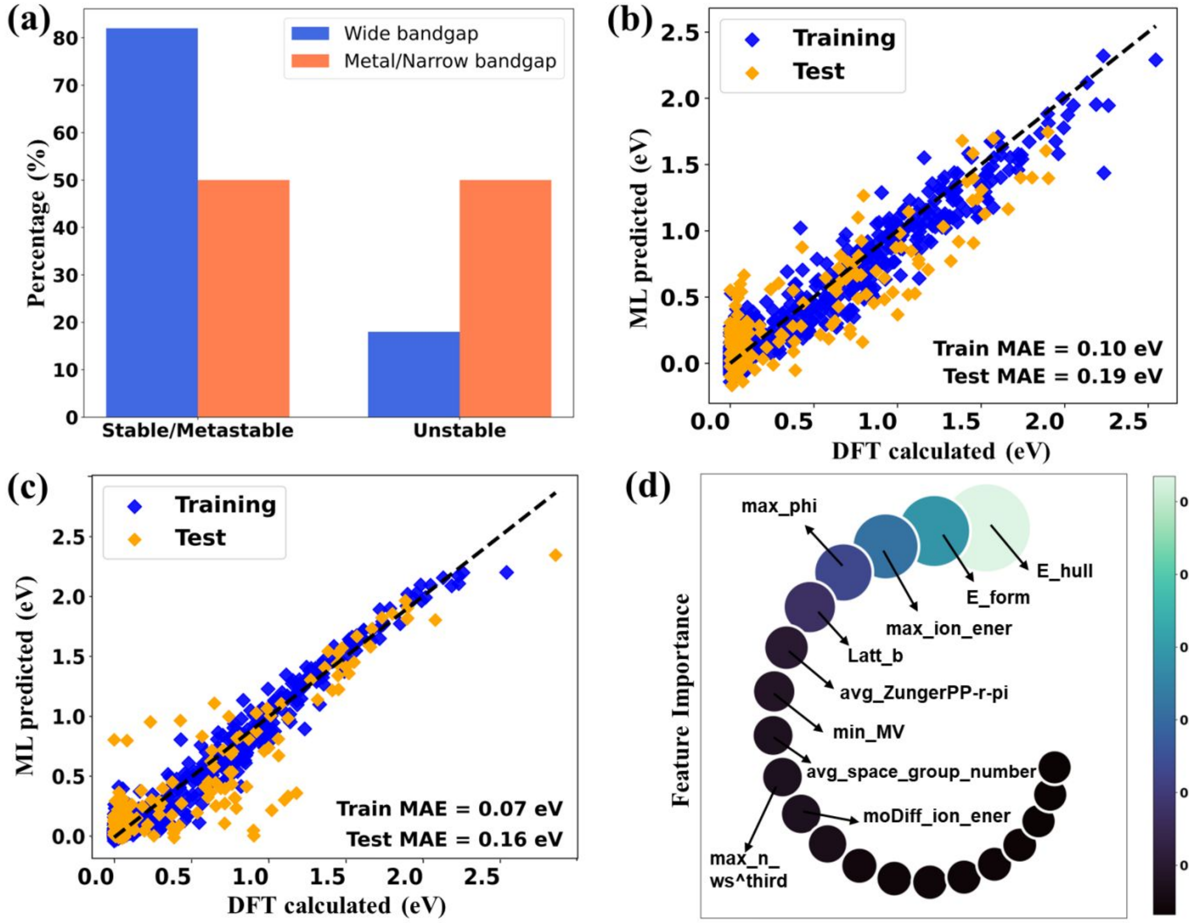

Figure 5: *(a) The stability, metastability, and instability distribution for semiconducting and metallic* $AMSe_3$ *compounds. Parity plots for high-fidelity HSE06 band gap prediction using (b) hist gradient boosting regressor model that includes* E_h *and* E_f *as features and (c) artificial neural network (ANN) model which relies on the GGA-PBE band gap as a feature. (d) Feature importance analysis for the band gap regression model as presented in (b), highlighting the key contributors to the prediction accuracy.*

ML models for band gap prediction: We train, cross-validate, and rigorously test several supervised regression models for predicting the high-fidelity HSE06 band gap of $AMSe_3$ with and without structural features (see Supplemental Section S5.1 for details). The best-performing ML model with only compositional and elemental features, achieves reasonable accuracy with a MAE of 0.24 eV (Supplemental Figure S9a), comparable to other reported band gap prediction models.[66–69] The large chemical space and relatively small dataset limit further improvements in prediction accuracy. In the next step, the models are trained and tested, including the lattice parameters as additional features. However, unlike stability prediction, incorporating structural information does not significantly improve the band gap prediction accuracy, indicating its relatively weak influence on electronic properties (Supplemental Figure S9b). To further improve the prediction accuracy, stability parameters E_f and E_h are incorporated as features for training the ML models. The best-trained hist gradient boosting regressor model achieves a reduced MAE of 0.19 eV for predicting high-fidelity HSE06 band gaps (Figure 5b).

Despite these improvements, we observe that traditional regression models plateaued in performance, likely due to their limited capacity to capture complex nonlinear relationships inherent in electronic property predictions. The band gap determination involves intricate interactions between atomic orbitals, electronic configuration, and quantum effects, which are not easily modeled by linear or even simple nonlinear regression techniques.[70] To address this challenge, we explore the use of artificial neural networks (ANNs), which are well-suited for modeling complex, nonlinear relationships due to their layered architecture and nonlinear activation functions.[71–73] ANNs can capture high-level abstractions and interactions between features that traditional models often miss. In our case, incorporating the low-fidelity GGA-PBE band gaps as a feature within an ANN framework allows the model to learn the nonlinear mapping between the inexpensive GGA-PBE calculations and the high-fidelity HSE06 band gaps efficiently. The ANN model exhibits the best performance with an MAE of 0.16 eV (Figure 5c), outperforming the regression models. This accurate predictive model surpasses the performance of several ML models reported previously. [66–69] The use of GGA-PBE band gaps, which are significantly faster (~80-85 times for our systems) to compute compared to hybrid HSE06 simulations, provides practical advantages. As most computational databases contain GGA-PBE band gaps, our developed ML models can readily be extended to predict more accurate HSE06-level band gaps for other material datasets.

Feature importance: The feature importance for hist gradient boosting regressor model reveals that E_f and E_h thermodynamic stability features are the most significant features for predicting the HSE06 band gaps of $AMSe_3$ (Figure 5d). Other elemental features like maximum ionization energy (max_ion_energy), maximum work function (max_phi) between A and M also rank highly in importance. The high feature importance for stability parameters is non-trivial. However, these stability features are somewhat correlate to the electronic properties of $AMSe_3$ as shown in Figure 5d. Moreover, the Spearman and Pearson Correlation analysis[74,75] reveals negative correlations between E_f or E_h and E_g, suggesting the lower or vanishing band gap for relatively less stable $AMSe_3$ compounds (Supplemental Figure S10a,b). For the best-performing ANN model, the feature importance predictably illustrates the much higher importance of the GGA-PBE band gap in predicting HSE06 counterparts (Supplemental Figure S11a). This is consistent with the strong correlation observed between GGA-PBE and HSE06 band gaps as shown in Supplemental Figure S11b.

***Materials screening with band gap*:** We apply the criterion $E_g > 0.5$ eV to further down-select thermodynamically stable $AMSe_3$ compounds for prototypical optoelectronic applications. Out of the initial 222 stable compounds, 137 $AMSe_3$ meet the band gap specification (Figure S12). Thus, the adopted dual-filtering strategy integrating thermodynamic stability with electronic performance, effectively narrows the candidate pool by ~85%, significantly accelerating the high-throughput materials screening process.

In the subsequent step, compounds with direct band gaps, which are usually desirable for optoelectronic applications, are identified. This screening step further narrows the number of potential candidates to 51 (Figure 4). The frequent indirect band gaps in NH_4CdCl_3-type AMX_3 (X = S, Se) can potentially originate from factors like MSe_6 tilting due to edge-sharing coordination and atomic orbital contribution to the band edge states.[21] The compositions of these screened $AMSe_3$ candidates remain broadly distributed across the periodic table (Figure 4).

Chemical trends in band gap and band edges: The projected density of states (pDOS) of $AMSe_3$ compounds depicts that the Se 4p orbitals mainly contribute to the valence band maximum (VBM), whereas the conduction band minimum (CBM) comprises contributions from Se 4p and M-site orbitals (Supplemental Figure S13). We further explore the chemical nature of band edge states of these screened selenides. $AMSe_3$ materials with transition metal as M-site exhibit CBM pre-dominantly composed of the *nd*-orbitals (n=3, 4, 5) (Supplemental Figure S13). Therefore, the band gap widens as M progresses from 3d to 4d to 5d elements. For example, $BMSe_3$ compounds have band gaps 1.34, 1.54, and 1.94 eV for M = Co (3d), Rh (4d), and Ir (5d), respectively (Supplemental Figure S14). A similar trend is observed for other transition metals, with Hf(5d) based selenides consistently exhibiting higher band gaps than Zr(4d) based ones, in agreement with findings reported by Sun et al.[22] (Supplemental Figure S15a) In other chemical spaces, compounds with non-metal M-sites construct the CBM from M-*np* and Se-*4p* orbitals (Figure 14b). Whereas the selenides with rare earth elements (e.g., Sc, La, and Y) as A and M, exhibit CBM states mostly contributed by *nd* orbitals (Supplemental Figure S15c). These results highlight the chemical versatility of the band edge states of NH_4CdCl_3-type $AMSe_3$ materials while maintaining optoelectronically suitable direct band gap (Supplemental Section S5.2). Additionally, the significant influence of M on electronic properties suggests that strategic alloying at the M-sites could be a promising approach for band gap tuning in ternary selenides, a strategy that has already been successfully demonstrated for sulfides.[32,34]

The band gaps of the screened $AMSe_3$ compounds align well with previously reported values from experimental and computational studies, as listed in Supplemental Table S3. For instance, Moroz *et al.* found an experimental band gap of 1.0 eV for $SrHfSe_3$, which matches our calculated HSE06 band gap.[30] The E_g data from other *in-silico* studies also agree with our calculations.[35]

Carrier effective masses

The efficient photogenerated charge separation and mobility are essential in high-performing optoelectronic materials. To simplify the evaluation process and avoid computationally intensive calculations, we focus on electron and hole carrier effective masses, m^*_e and m^*_h, that are inversely related to their corresponding carrier mobilities, μ_e and μ_h (Supplemental Section S1). Optoelectronically promising materials are expected to possess smaller $m^*_{e/h}$, typically indicative of superior transport characteristics.[76–79] To refine the candidate pool, we choose the most frequently considered criteria of $m^*_e < 1.0$ and $m^*_h < 1.0$, identifying ternary selenides with low electron and hole masses. This crucial screening step leads to 30 candidates with suitable carrier transport characteristics (Supplemental Table S4).

Light absorbance on the context of photovoltaic performance metric

For the subsequent screening step, we compute the Spectroscopic Limited Maximum Efficiency (SLME) of screened $AMSe_3$ candidates to assess their light absorption potential, for example when serving as the absorbing layer for solar cells. The SLME represents the highest achievable efficiency of a light-absorbing material and can be considered the theoretical maximum photoconversion efficiency of a single p–n junction solar cell.[80]

We set the selection criterion as SLME >22% (for a film thickness of 1 μm), resulting in the identification of 22 $AMSe_3$ materials with promising power conversion efficiencies. The higher SLME threshold compared to other studies guarantees the promising photovoltaic properties of screened materials.[81,82] As depicted in Figure 6a, these screened materials achieve SLME values ranging from 22.8% to 30.1%, surpassing many other well-explored higher efficiency light absorbers.[81] The dense electronic states at the band edges of these selenides result in strong optical absorption, as shown in Supplemental Figure S16, ultimately boosting their power conversion efficiency.

Elemental Toxicity

In the following step, we implement a stringent refinement step to evaluate the environmental and health implications of the screened compounds. Recognizing the potential hazards associated with certain elements, we exclude compounds containing Arsenic (As) and Lanthanum (La) from further consideration (marked with a cross in Figure 6a). This refinement ensures that the final selection includes compounds both excelling in efficiency and stability, and adhering to strict safety and environmental standards. As a result, 17 ternary selenides with high SLME are toxic-element free and should not directly pose environmental threats. Note that, the discarded compounds can reduce the concentration of toxic elements through compositional engineering without compromising photovoltaic characteristics. This strategy has been successfully demonstrated for toxic Pb-based halide perovskites.[18,83]

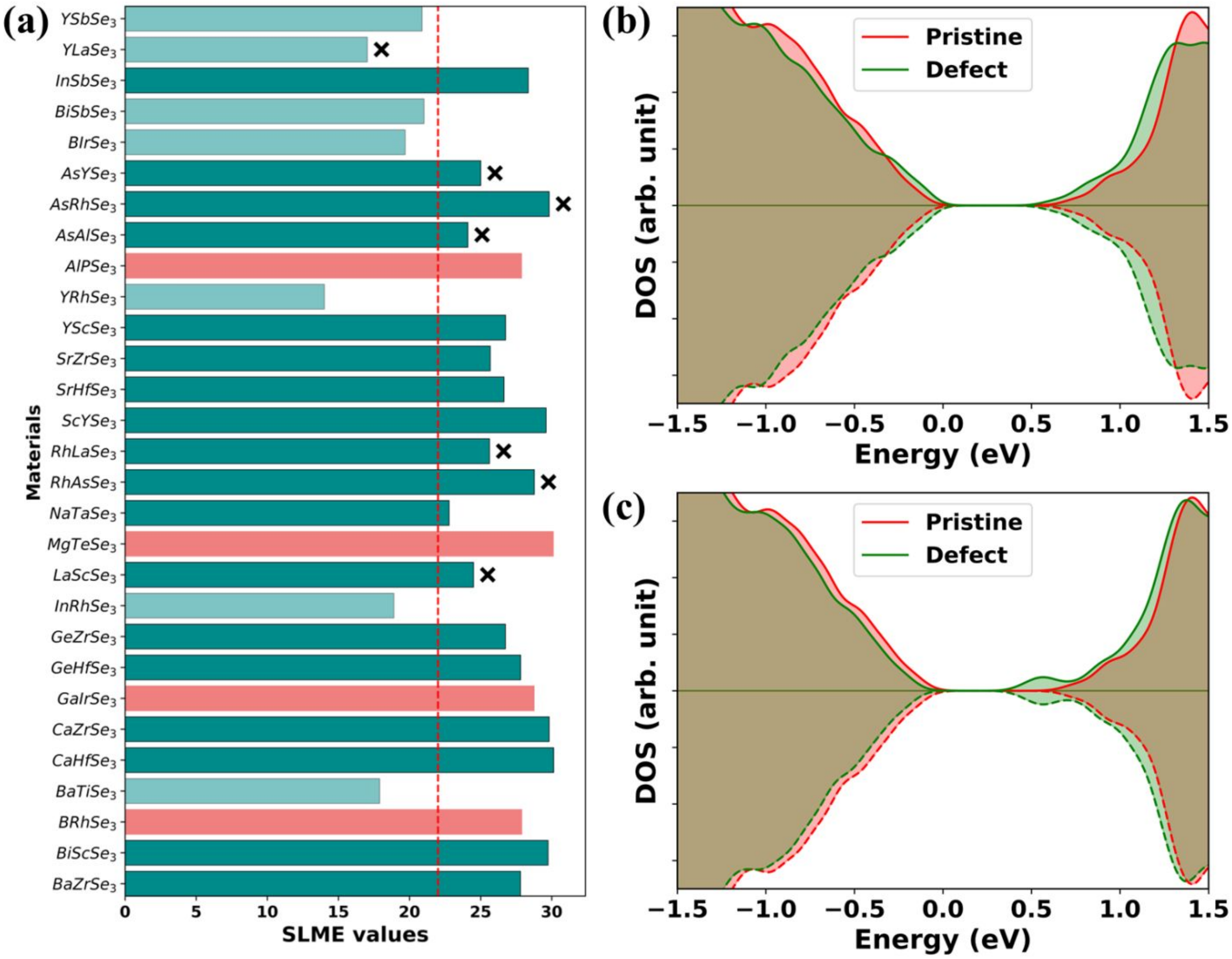

Figure 6: *(a) SLME values of 30 $AMSe_3$ compounds with low effective masses. The '×' symbol marks $AMSe_3$ materials that contain toxic elements. The ternary selenides with red bar indicate their potential phase instability compared to other competing phases. The spin-polarized density of states for (b) $CaZrSe_3$ and (c) $BRhSe_3$ with neutral selenide defects are also presented. In contrast to $BRhSe_3$, all defect levels for $CaZrSe_3$ lie within 0.1 eV of the band-edge states and can be considered as shallow defect states.*

Phase stability

We next explore the thermodynamic phase stability of screened $AMSe_3$ materials. As detailed in Supplemental Section S1, the total energies of these compounds are calculated across all commonly reported prototypical crystal structures (Figure 1a). Consistent to our initial findings, the edge-sharing orthorhombic P*nma* phase emerges as the most stable structure for most of the cases (12 out of 17 or 71%) (Supplemental Table S5). Ternary selenides that exhibit stable phases other than the NH_4CdCl_3-type are marked with red bars in Figure 6a. These results validate our initial approach of considering only the most frequently stable phase, which substantially reduces the computational expense and accelerates the screening process.

Defect-tolerance

The screened candidates are further scrutinized to elucidate their point-defect resilience. Point-defect-induced in-gap states frequently degrades optical performance of semiconductors. These additional electronic states may act as recombination centers and become traps for photo-generated carriers (electrons and holes), which in turn degrades carrier mobility, shortens its lifetime, and reduces charge separation efficiency.

We consider atomic vacancy defects, including A, M, and Se vacancies, which often exhibit low defect-formation energies. Our goal is to qualitatively assess the presence of deep-defect states, focusing exclusively on neutral defects to establish a clear foundation without the added complexity of charged states. While the use of a semi-local exchange–correlation functional introduces some limitations, such as band gap underestimation and delocalization errors, it provides an efficient and reliable starting point for identifying key trends in defect behavior. Other defect types, such as anion interstitials and cation anti-site defects, can significantly determine the defect tolerance and overall optoelectronic performance of chalcogenide materials, particularly in complex ternary and quaternary systems.[84] Advanced methods like hybrid functionals or GW calculations, while capable of greater accuracy, are better suited for future studies aiming to resolve defect levels with higher precision.

The pDOS plots in Figure 6b-c and Supplemental Figure S17 summarize the defect properties of $AMSe_3$ compounds. Seven defect-tolerant candidates are standing out that they do not introduce deep trap levels despite hosting A, M, and Se vacancies. For instance, as shown in Figure 6b and Supplemental Figure S17, the defect arising from Ca, Zr, and Se vacancies in $CaZrSe_3$ do not create in-gap states. Meanwhile, $BRhSe_3$ material shows defect intolerance as the Se-defects introduce deep trap levels within the band gap (Figure 6c). Since anion vacancies primarily contribute to deep defect states, mitigating such defects can improve characteristics of these ternary selenides. These seven $AMSe_3$ candidates, as summarized in Table 1, emerge as the final materials that we find highly promising for photovoltaic applications. A brief overview of our multi-step screening process and the number of surviving $ABSe_3$ compounds after each step is schematically shown in Figure 7.

Among the screened materials, polycrystalline $SrHfSe_3$ and $SrZrSe_3$ have already been synthesized and structurally characterized in the NH_4CdCl_3-type phase.[30,63] However, transport measurements and optoelectronic device fabrications from these materials have yet to be reported. We also note that sulfur analogs of most of these final $AMSe_3$ compounds have been experimentally synthesized.[21,85] With the rapid recent advancements in low-temperature synthetic routes for ternary chalcogenides, we anticipate that the remaining selenides will be realized soon.[21]

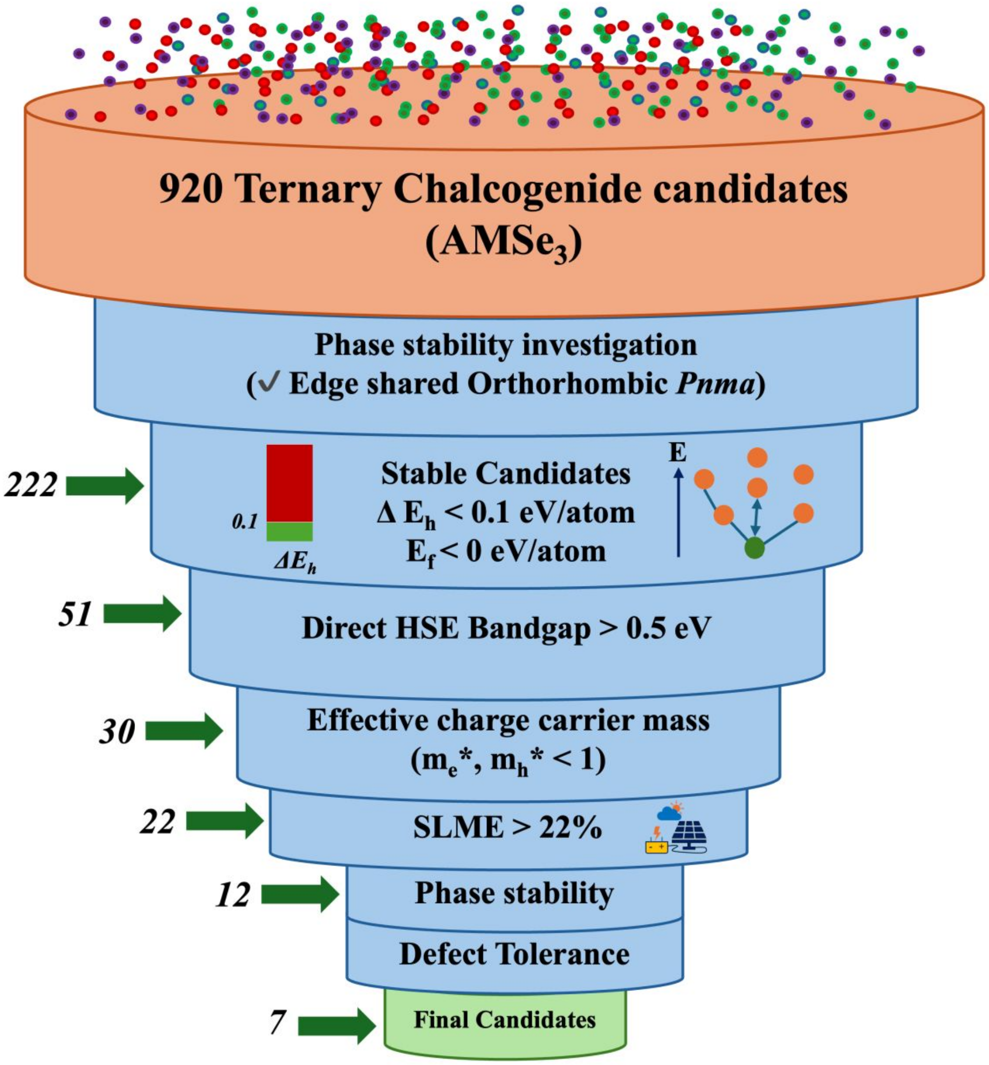

Figure 7. *Procedural outline of the multi-step screening process employed to select AMSe$_3$ with promising optoelectronic properties.*

Table 1: *Characteristics of the final seven AMSe₃ candidates pertinent to their potential photovoltaic applications.*

Compound	HSE06 Band gap (eV)	m_e*	m_h*	SLME (%) (1 µm)
$BaZrSe_3$	0.99	0.482	-0.587	27.80
$CaZrSe_3$	1.11	0.479	-0.306	29.81
$GeZrSe_3$	0.85	0.406	-0.525	26.74
$ScYSe_3$	1.43	0.569	-0.639	29.60
$SrHfSe_3$	1.0	0.401	-0.536	26.64
$SrZrSe_3$	0.84	0.968	-0.558	25.67
$YScSe_3$	0.96	0.679	-0.63	26.75

Thin-film photovoltaics

The thickness-dependent SLME in Supplemental Figure S18 depicts that the final candidates reach near-maximum conversion efficiency within 1 µm of thickness, suggesting their potential application in thin-film solar cells. Thin absorbing layers enable photogenerated carriers to traverse shorter distances to reach the contacts, thereby reducing their recombination losses. We note that conventional thin-film absorbers like GaAs usually require thickness greater than 2 µm to absorb enough sunlight.[86,87] Thus, the thinner absorbing layers of these newly explored ternary selenides can introduce solar cells with better structural flexibility and affordability compared to currently commercialized technologies.

Structural Integrity

To confirm the dynamic stability of selected candidates, we performed phonon calculations on our selected candidates, as depicted in Figure S19. Moreover, to evaluate the structural integrity and thermal stability of screened $AMSe_3$ compounds, we employ *ab initio* molecular dynamics (AIMD) simulations under ambient conditions, as detailed in Supplemental Section S1. Given the heavy computational expense, the current study explores three representative compounds with high SLME: $BaZrSe_3$, $ScYSe_3$, and $SrHfSe_3$. These candidates are selected to represent distinct A and M elements and address different chemical spaces. Figure 8a illustrates that the potential energies of these materials fluctuate around their average values over time and remain confined within a narrow range despite inherent structural distortions. The temperatures over time in these systems also fluctuate around the desired value, 300 K, see Supplemental Figure S20. The selected snapshots of $AMSe_3$ structures confirm their robustness, see inset in Figures 8a and Supplemental Figure S21. To further assess the structural rigidity of the $AMSe_3$ compounds, we calculate the pair distribution functions (g(r)) for M–Se bonds. As depicted in Figure 8b, the g(r) profiles exhibit sharp peaks, signifying well-maintained atomic arrangements in the edge-sharing orthorhombic structures at 300 K. Overall, our AIMD simulations confirm the strong bonding interactions and structural integrity of the ternary selenides, validating their thermal stability.

Excited Carrier Dynamics and Lifetime

Finally, we study the excited carrier dynamics and non-radiative recombination processes under ambient conditions in these three $AMSe_3$ compounds. The time-domain Density Functional Theory (TD-DFT) combined with Non-Adiabatic Molecular Dynamics (NAMD) simulations are utilized to evaluate the charge carrier lifetime, a key parameter for photovoltaic performance.[88] As detailed in Supplemental Section S1, these methods qualitatively track the time-dependent increase in carrier population in the ground state due to non-radiative charge recombination across the band gap. The rate of population growth is inversely proportional to the photoexcited carrier lifetime. Figure 8c reveals calculated slow non-radiative carrier relaxation rates in these $AMSe_3$ compounds, evidencing potential long carrier lifetimes in the excited state. The calculated lifetimes for $BaZrSe_3$, $ScYSe_3$, and $SrHfSe_3$ are 2.1, 4.2, and 1.18 ns, respectively. The photoexcited lifetimes on the nanosecond scale are quite comparable to the measured values for other inorganic materials, including halide perovskites like $CsPbBr_3$ (Table 2). [89,90]

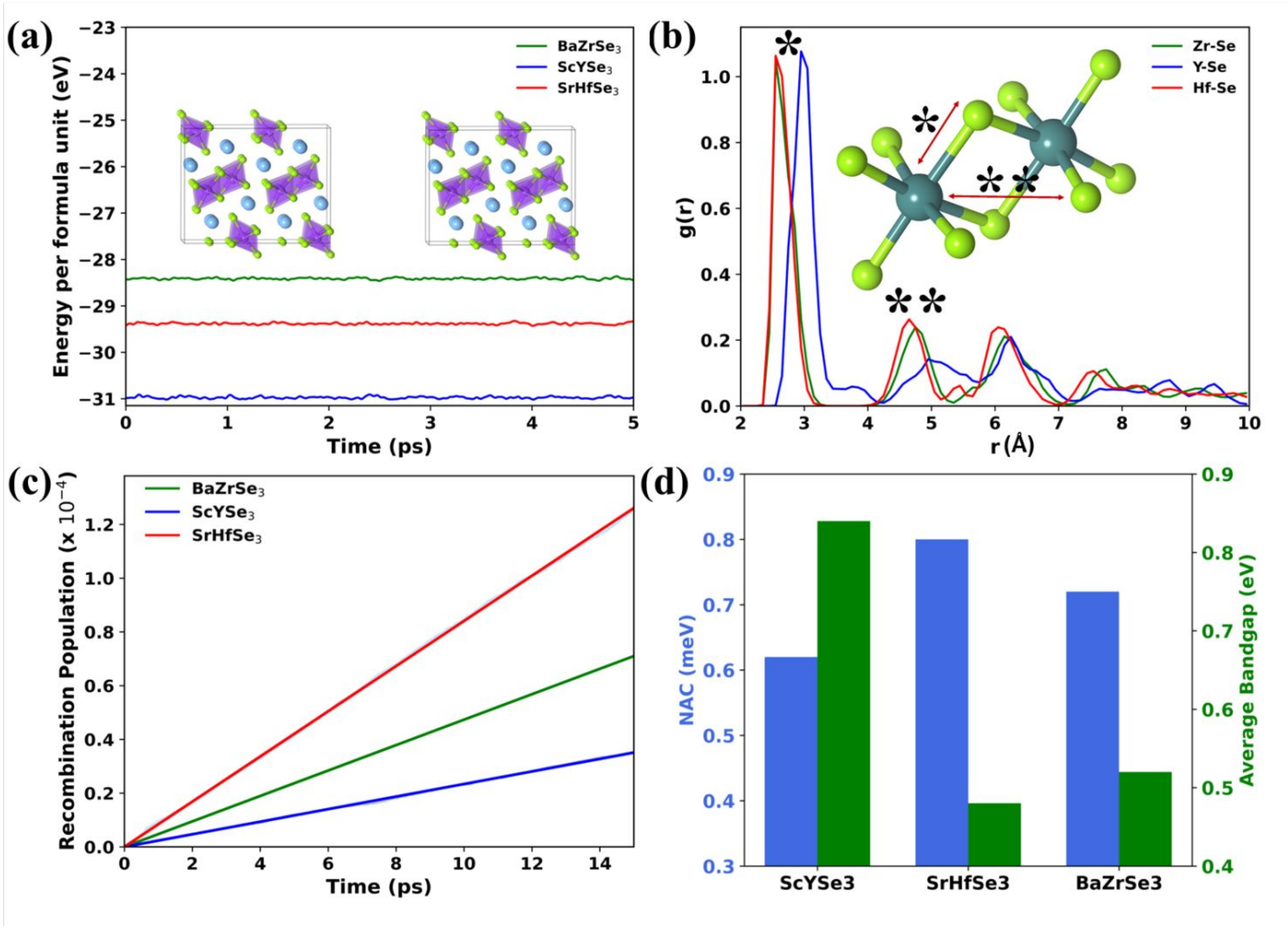

Figure 8. *The structural stability of three representative $AMSe_3$ systems, $BaZrSe_3$, $ScYSe_3$, and $SrHfSe_3$, evaluated at 300K. (a) The total energy per formula unit of three $AMSe_3$, where variations reflect thermal fluctuation at a narrow energy range, (b) The g(r) of M-Se feature sharp peaks*

evidencing the retained material crystallinity at 300K, (c) The time-dependent population of non-radiatively recombined electron-hole pairs. The function f(t) = 1 - exp(-t/τ) is used to fit the population rise with time; here τ is the effective electron-hole recombination time. (d) Average NAC values and calculated average band gap for these compounds.

The band gap variations and non-adiabatic coupling (NAC) strengths under ambient conditions are known to decisively impact photoexcited carrier lifetimes in semiconductors.[91,92] Figure 8d depicts the time-average band gaps and NAC values closely correlating with the observed trend in carrier lifetimes for $SrHfSe_3$, $BaZrSe_3$, and $ScYSe_3$. Among these three candidates, the highest band gap and the weakest NAC give rise to the longest carrier lifetime in $ScYSe_3$. During non-radiative carrier relaxation and recombination, the photoexcited carriers dissipate excess energy via electron-phonon coupling, exciting various lattice phonon modes. Higher band gap and weak NACs in $ScYSe_3$ partially suppress such energy dissipation process, extending the excited state lifetime. More details on modeling of carrier dynamics and recombination processes are provided in Supplemental Section S8.

Table 2: Comparison of non-radiative carrier lifetime of representative systems.

	$BaZrSe_3$	**$ScYSe_3$**	**$SrHfSe_3$**	**$CsPbBr_3$** [89]
Recombination lifetime (ns)	2.1	4.2	1.18	1.45

Discussion

Ternary chalcogenides are often explored to search for stable materials in conventionally photoactive phases featuring corner-shared MSe_6 octahedra. However, a comprehensive exploration over available chemical space reveals the exciting photoactivity and carrier transport characteristics of $AMSe_3$ emerging in an often thermodynamically stable NH_4CdCl_3-type orthorhombic phase. High-quality films or single crystals of these selenides can eventually enable promising optoelectronic devices with long-term stability. In this regard, robust ambient stability of chalcogenides at room temperature suggests less extensive post-processing of these materials for practical device applications.

Our accurate ML models reveal the most crucial elemental and structural features that substantially control the $AMSe_3$ material stability and its fundamental electronic properties. These insights are useful for further tuning the core material properties through compositional engineering. For example, the high feature importance of lattice parameters in stability and band gap prediction models suggests that applying controlled lattice strain in $AMSe_3$ could be an effective tool for modifying these characteristics. Lattice compression and expansion have already been extensively used to optimize the optoelectronic properties of photoactive materials including chalcogenides,[93,94] highlighting the potential of this approach for $AMSe_3$ systems.

In this study we have highlighted our procedure to down select materials suitable for solar cell application given well established performance metric for photovoltaic. In addition to their potential in photovoltaics, ternary selenides show a remarkable versatility across several other optoelectronic and energy-related applications. For instance, light-emitting diodes (LEDs) represent a promising avenue, where the impressive luminescent properties, efficient carrier transport, defect tolerance, and robust environmental stability of these $AMSe_3$ can make them superior candidates.[95] Moreover, due to efficient photo-excited electron-hole pair generation and suitable band alignments, these chalcogenides can be promising photocatalysts for various chemical reactions.[96] Furthermore, these ternary selenides can be suitable for photochemical water splitting owing to their wide band gaps (~2 eV) and high carrier mobilities. In this context, Kuhar et al. investigated sulfide analogue AMS_3 and proposed a few candidates as potential water-splitting materials with wide band gaps.[19] $AMSe_3$ compounds also exhibit features such as low lattice thermal conductivity, which makes them suitable for thermoelectric applications. Cao et al. identified quasi-ductile thermoelectric compounds, reporting six n-type and six p-type candidates with $ZT>0.3$ at 300K.[97] The high-quality dataset presented here as separate file can readily be used to screen ternary selenides for other targeted applications.

Conclusions

In conclusion, our study introduces an advanced data-driven framework, integrated with high-throughput *ab initio* simulations, to systematically screen ternary selenides for optoelectronic applications. Among several common polymorphs, the edge-shared orthorhombic NH_4CdCl_3-type phase (*Pnma*) emerges as the most frequently stable structure for $AMSe_3$ compounds. By exploring the relevant chemical space, we develop and publish an extensive *in-silico* dataset comprising optimal geometries and high-fidelity electronic structures for 920 candidates in this orthorhombic phase. Reliable supervised ML models are trained and tested for accelerated screening, using thermodynamic stability parameters and electronic band gap values as criteria. Feature importance analysis from these models suggests specific design approaches to boost the stability and key photovoltaic properties of ternary selenides. We further establish a multi-tiered high-throughput materials screening workflow incorporating stringent materials characteristics. This systematic screening identifies tenths of new ternary selenides with desired functional properties such as hull stability, direct band gap spanning a wide range, low charge carrier mass, and high SLME. Our staged selection process finally identifies seven $AMSe_3$ compounds with promising photovoltaic properties. The AIMD and NAMD simulations on three of these selenides reveal their thermal stability and long carrier lifetimes, indicating their potential optoelectronic applications. This application screens materials suitable for photovoltaics. However, we note that exceptional functional properties of $AMSe_3$ materials suggest their versatility in a wide variety of applications ranging from photocatalysis to light emission to thermoelectric. This work emphasizes the importance of exploring traditionally overlooked but thermodynamically stable non-perovskite phases of ternary chalcogenides to uncover their exciting functional characteristics for advanced optoelectronic technologies.

Methods:

In this work, all the DFT-based calculations and AIMD simulations were performed using the Vienna Ab Initio Simulation Package (VASP).[98,99] The Perdew−Burke−Ernzerhof (PBE) version of the exchange-correlation functional[100] within the Generalized Gradient Approximation (GGA), projector-augmented wave (PAW)[101] method and the plane wave basis sets[102] were employed for structure relaxation and other static calculations. In some instances, the hybrid HSE06 functional [103,104] was employed to determine the band gaps of ternary selenides, aiming for quantitative agreement with experimental values. Geometric relaxation of the structures was performed using the PBE functional. Crystal structures were optimized with an energy convergence criterion of 1×10^{-5} eV, employing a kinetic energy cutoff of 400 eV for the plane-wave basis. Relaxation of structures continued until atomic forces reached below 0.04 eV/Å. To ensure consistency and accuracy in formation energy and convex hull calculations, parameters identical to those in the OQMD[105] dataset were adopted. Spin-polarization was explicitly included in all calculations to account for the magnetic effects of 3d-transition metal elements. However, spin-orbit coupling (SOC) was not considered due to the significant computational cost associated with high-throughput calculations of the large $AMSe_3$ dataset.

To ensure a consistent and accurate description of the $AMSe_3$ compounds, we employed the HSE06 hybrid functional, which is well-known for reliably capturing the electronic structure of transition metal chalcogenides without the need for empirical Hubbard U corrections.[106] While the inclusion of Hubbard U parameters can improve the localization of d-electrons, their selection is highly system-dependent and requires rigorous benchmarking. This makes their application impractical for high-throughput computational studies. Specific details about various types of calculations – convex hull distance, formation Energy, effective charge carrier masses, SLME, phase stability, defect calculations, phonon calculations, AIMD, and NAMD are given in Supplemental Section S1(a).

The machine learning methodology for predicting the thermodynamic stability of ternary selenides involves constructing a dataset with 348 features from elemental properties (MAGPIE)[107] and structural attributes. Feature engineering eliminates features with >10% missing data, low variance, or high correlation (≥0.95), and selects relevant ones using Recursive Feature Elimination (RFE).[108] Regression and classification tasks predict formation energy, hull distance, and band gap, with an 80/20 train-test split. Baseline models are tested with Lazy Predict, followed by hyperparameter tuning and advanced models like artificial neural networks (ANN).

Permutation Feature Importance identifies key features driving model performance. Further details on data science computational methods are included in Supplemental Section S1(b).

Acknowledgements

D.G. acknowledges the IIT Delhi SEED Grant (PLN12/04MS), the Science and Engineering Research Board (SERB), Department of Science and Technology (DST), India for Start-up Research Grant SRG/2022/001234, CSIR-Human Resource Development Group (HRDG) for ExtraMural Research-II Grant 01/3136/23/EMR-II and the IIT Delhi HPC facility for computational resources. The research presented in this article was supported by the Laboratory Directed Research and Development program of Los Alamos National Laboratory (LANL) under project number 20190656PRD4 and 20240590ECR. This work was performed in part at the Center for Integrated Nanotechnology (CINT) at LANL, a U.S. DOE and Office of Basic Energy Sciences user facility. This research used resources provided by the LANL Institutional Computing Program. LANL is operated by Triad National Security, LLC, for the National Nuclear Security Administration of U.S. Department of Energy (Contract No. 89233218CNA000001).

References:

(1) Johnston, A.; Sargent, E. H. Accelerated Discovery of Optoelectronic Materials. *ACS Photonics* **2021**, *8* (3), 699–701. https://doi.org/10.1021/acsphotonics.0c01949.

(2) A Decade of Perovskite Photovoltaics. *Nat Energy* **2019**, *4* (1), 1–1. https://doi.org/10.1038/s41560-018-0323-9.

(3) Li, L.; Fan, Z. Optoelectronic Materials and Devices. *Small Methods* **2024**, *8* (2). https://doi.org/10.1002/smtd.202301632.

(4) Manser, J. S.; Christians, J. A.; Kamat, P. V. Intriguing Optoelectronic Properties of Metal Halide Perovskites. *Chem Rev* **2016**, *116* (21), 12956–13008. https://doi.org/10.1021/acs.chemrev.6b00136.

(5) Wu, X. High-Efficiency Polycrystalline CdTe Thin-Film Solar Cells. *Solar Energy* **2004**, *77* (6), 803–814. https://doi.org/10.1016/j.solener.2004.06.006.

(6) Scandale, W.; Still, D. A.; Carnera, A.; Della Mea, G.; De Salvador, D.; Milan, R.; Vomiero, A.; Baricordi, S.; Dalpiaz, P.; Fiorini, M.; Guidi, V.; Martinelli, G.; Mazzolari, A.; Milan, E.; Ambrosi, G.; Azzarello, P.; Battiston, R.; Bertucci, B.; Burger, W. J.; Ionica, M.; Zuccon, P.; Cavoto, G.; Santacesaria, R.; Valente, P.; Vallazza, E.; Afonin, A. G.; Baranov, V. T.; Chesnokov, Y. A.; Kotov, V. I.; Maisheev, V. A.; Yaznin, I. A.; Afansiev, S. V.; Kovalenko, A. D.; Taratin, A. M.; Denisov, A. S.; Gavrikov, Y. A.; Ivanov, Y. M.; Ivochkin, V. G.; Kosyanenko, S. V.; Petrunin, A. A.; Skorobogatov, V. V.; Suvorov, V. M.; Bolognini, D.; Foggetta, L.; Hasan, S.; Prest, M. High-Efficiency Volume Reflection of an Ultrarelativistic Proton Beam with a Bent Silicon Crystal. *Phys Rev Lett* **2007**, *98* (15), 154801. https://doi.org/10.1103/PhysRevLett.98.154801.

(7) Barbato, M.; Artegiani, E.; Bertoncello, M.; Meneghini, M.; Trivellin, N.; Mantoan, E.; Romeo, A.; Mura, G.; Ortolani, L.; Zanoni, E.; Meneghesso, G. CdTe Solar Cells: Technology, Operation and Reliability. *J Phys D Appl Phys* **2021**, *54* (33), 333002. https://doi.org/10.1088/1361-6463/ac04e3.

(8) Morkoç, H.; Strite, S.; Gao, G. B.; Lin, M. E.; Sverdlov, B.; Burns, M. Large-Band-Gap SiC, III-V Nitride, and II-VI ZnSe-Based Semiconductor Device Technologies. *J Appl Phys* **1994**, *76* (3), 1363–1398. https://doi.org/10.1063/1.358463.

(9) Lester, S. D.; Ponce, F. A.; Craford, M. G.; Steigerwald, D. A. High Dislocation Densities in High Efficiency GaN-Based Light-Emitting Diodes. *Appl Phys Lett* **1995**, *66* (10), 1249–1251. https://doi.org/10.1063/1.113252.

(10) Hegedus, S. Thin Film Solar Modules: The Low Cost, High Throughput and Versatile Alternative to Si Wafers. *Progress in Photovoltaics: Research and Applications* **2006**, *14* (5), 393–411. https://doi.org/10.1002/pip.704.

(11) Lin, Y.; Li, Y.; Zhan, X. Small Molecule Semiconductors for High-Efficiency Organic Photovoltaics. *Chem Soc Rev* **2012**, *41* (11), 4245. https://doi.org/10.1039/c2cs15313k.

(12) Shi, J.; Zhang, J.; Yang, L.; Qu, M.; Qi, D.; Zhang, K. H. L. Wide Bandgap Oxide Semiconductors: From Materials Physics to Optoelectronic Devices. *Advanced Materials* **2021**, *33* (50). https://doi.org/10.1002/adma.202006230.

(13) Li, X.; Yang, J.; Jiang, Q.; Lai, H.; Li, S.; Tan, Y.; Chen, Y.; Li, S. Perovskite Solar Cells Employing an Eco-Friendly and Low-Cost Inorganic Hole Transport Layer for Enhanced Photovoltaic Performance and Operational Stability. *J Mater Chem A Mater* **2019**, *7* (12), 7065–7073. https://doi.org/10.1039/C9TA01499C.

(14) Swarnkar, A.; Mir, W. J.; Chakraborty, R.; Jagadeeswararao, M.; Sheikh, T.; Nag, A. Are Chalcogenide Perovskites an Emerging Class of Semiconductors for Optoelectronic Properties and Solar Cell? *Chemistry of Materials* **2019**, *31* (3), 565–575. https://doi.org/10.1021/acs.chemmater.8b04178.

(15) Syafiq, U.; Isotta, E.; Ataollahi, N.; Lohani, K.; Luong, S.; Trifiletti, V.; Fenwick, O.; Scardi, P. Facile and Low-Cost Fabrication of Cu/Zn/Sn-Based Ternary and Quaternary Chalcogenides Thermoelectric Generators. *ACS Appl Energy Mater* **2022**, *5* (5), 5909–5918. https://doi.org/10.1021/acsaem.2c00268.

(16) Wang, R.; Huang, T.; Xue, J.; Tong, J.; Zhu, K.; Yang, Y. Prospects for Metal Halide Perovskite-Based Tandem Solar Cells. *Nat Photonics* **2021**, *15* (6), 411–425. https://doi.org/10.1038/s41566-021-00809-8.

(17) Qiu, L.; He, S.; Ono, L. K.; Liu, S.; Qi, Y. Scalable Fabrication of Metal Halide Perovskite Solar Cells and Modules. *ACS Energy Lett* **2019**, *4* (9), 2147–2167. https://doi.org/10.1021/acsenergylett.9b01396.

(18) Zhu, Y.; Kang, Y.; Huang, H.; Zhuang, D.; Li, M.; Ling, Z.; Peng, K.; Zhai, L.; Zou, C. Systematic Evaluation of the Biotoxicity of Pb-Based Perovskite Materials and Perovskite Solar Cells. *J Mater Chem A Mater* **2024**, *12* (5), 2916–2923. https://doi.org/10.1039/D3TA06303H.

(19) Kuhar, K.; Crovetto, A.; Pandey, M.; Thygesen, K. S.; Seger, B.; Vesborg, P. C. K.; Hansen, O.; Chorkendorff, I.; Jacobsen, K. W. Sulfide Perovskites for Solar Energy Conversion Applications: Computational Screening and Synthesis of the Selected Compound $LaYS_3$. *Energy Environ Sci* **2017**, *10* (12), 2579–2593. https://doi.org/10.1039/C7EE02702H.

(20) Shen, C.; Li, T.; Zhang, Y.; Xie, R.; Long, T.; Fortunato, N. M.; Liang, F.; Dai, M.; Shen, J.; Wolverton, C. M.; Zhang, H. Accelerated Screening of Ternary Chalcogenides for Potential Photovoltaic Applications. *J Am Chem Soc* **2023**, *145* (40), 21925–21936. https://doi.org/10.1021/jacs.3c06207.

(21) Han, Y.; Fang, X.; Shi, Z. Advances in Chalcogenide Perovskites: Fundamentals and Applications. *Appl Phys Rev* **2024**, *11* (2). https://doi.org/10.1063/5.0203535.

(22) Sun, Y.-Y.; Agiorgousis, M. L.; Zhang, P.; Zhang, S. Chalcogenide Perovskites for Photovoltaics. *Nano Lett* **2015**, *15* (1), 581–585. https://doi.org/10.1021/nl504046x.

(23) Kuhar, K.; Crovetto, A.; Pandey, M.; Thygesen, K. S.; Seger, B.; Vesborg, P. C. K.; Hansen, O.; Chorkendorff, I.; Jacobsen, K. W. Sulfide Perovskites for Solar Energy Conversion Applications: Computational Screening and Synthesis of the Selected Compound $LaYS_3$. *Energy Environ Sci* **2017**, *10* (12), 2579–2593. https://doi.org/10.1039/C7EE02702H.

(24) Zhang, H.; Wu, X.; Ding, K.; Xie, L.; Yang, K.; Ming, C.; Bai, S.; Zeng, H.; Zhang, S.; Sun, Y.-Y. Prediction and Synthesis of a Selenide Perovskite for Optoelectronics. *Chemistry of Materials* **2023**, *35* (11), 4128–4135. https://doi.org/10.1021/acs.chemmater.2c03676.

(25) Han, Y.; Xu, J.; Liang, Y.; Chen, X.; Jia, M.; Zhang, J.; Lian, L.; Liu, Y.; Li, X.; Shi, Z. P-Type Conductive BaZrS3 Thin Film and Its Band Gap Tunning via Ruddlesden-Popper Ba3Zr2S7 and Titanium Alloying. *Chemical Engineering Journal* **2023**, *473*, 145351. https://doi.org/10.1016/j.cej.2023.145351.

(26) Wei, X.; Hui, H.; Zhao, C.; Deng, C.; Han, M.; Yu, Z.; Sheng, A.; Roy, P.; Chen, A.; Lin, J.; Watson, D. F.; Sun, Y.-Y.; Thomay, T.; Yang, S.; Jia, Q.; Zhang, S.; Zeng, H. Realization of BaZrS3 Chalcogenide Perovskite Thin Films for Optoelectronics. *Nano Energy* **2020**, *68*, 104317. https://doi.org/10.1016/j.nanoen.2019.104317.

(27) Sadeghi, I.; Ye, K.; Xu, M.; Li, Y.; LeBeau, J. M.; Jaramillo, R. Making $BaZrS_3$ Chalcogenide Perovskite Thin Films by Molecular Beam Epitaxy. *Adv Funct Mater* **2021**, *31* (45). https://doi.org/10.1002/adfm.202105563.

(28) Gupta, T.; Ghoshal, D.; Yoshimura, A.; Basu, S.; Chow, P. K.; Lakhnot, A. S.; Pandey, J.; Warrender, J. M.; Efstathiadis, H.; Soni, A.; Osei-Agyemang, E.; Balasubramanian, G.; Zhang, S.; Shi, S.; Lu, T.; Meunier, V.; Koratkar, N. An Environmentally Stable and Lead-Free Chalcogenide Perovskite. *Adv Funct Mater* **2020**, *30* (23). https://doi.org/10.1002/adfm.202001387.

(29) Niu, S.; Huyan, H.; Liu, Y.; Yeung, M.; Ye, K.; Blankemeier, L.; Orvis, T.; Sarkar, D.; Singh, D. J.; Kapadia, R.; Ravichandran, J. Bandgap Control via Structural and Chemical Tuning of Transition Metal Perovskite Chalcogenides. *Advanced Materials* **2017**, *29* (9). https://doi.org/10.1002/adma.201604733.

(30) Moroz, N. A.; Bauer, C.; Williams, L.; Olvera, A.; Casamento, J.; Page, A. A.; Bailey, T. P.; Weiland, A.; Stoyko, S. S.; Kioupakis, E.; Uher, C.; Aitken, J. A.; Poudeu, P. F. P. Insights on the Synthesis, Crystal and Electronic Structures, and Optical and Thermoelectric Properties of Sr1–XSbxHfSe3. *Inorg Chem* **2018**, *57* (12), 7402–7411. https://doi.org/10.1021/acs.inorgchem.8b01038.

(31) Sadeghi, I.; Ye, K.; Xu, M.; Li, Y.; LeBeau, J. M.; Jaramillo, R. Making $BaZrS_3$ Chalcogenide Perovskite Thin Films by Molecular Beam Epitaxy. *Adv Funct Mater* **2021**, *31* (45). https://doi.org/10.1002/adfm.202105563.

(32) Meng, W.; Saparov, B.; Hong, F.; Wang, J.; Mitzi, D. B.; Yan, Y. Alloying and Defect Control within Chalcogenide Perovskites for Optimized Photovoltaic Application. *Chemistry of Materials* **2016**, *28* (3), 821–829. https://doi.org/10.1021/acs.chemmater.5b04213.

(33) Ong, M.; Guzman, D. M.; Campbell, Q.; Dabo, I.; Jishi, R. A. BaZrSe3: *Ab Initio* Study of Anion Substitution for Bandgap Tuning in a Chalcogenide Material. *J Appl Phys* **2019**, *125* (23). https://doi.org/10.1063/1.5097940.

(34) Kanoun, M. B.; Ul Haq, B.; Kanoun, A.-A.; Goumri-Said, S. Ti Alloying as a Route to $BaZrS_3$ Chalcogenide Perovskite with Enhanced Photovoltaic Performance. *Energy & Fuels* **2023**, *37* (13), 9548–9556. https://doi.org/10.1021/acs.energyfuels.3c01272.

(35) Adhikari, S.; Johari, P. Photovoltaic Properties of ABSe3 Chalcogenide Perovskites (*A* = Ca, Sr, Ba; *B* = Zr, Hf). *Phys Rev B* **2024**, *109* (17), 174114. https://doi.org/10.1103/PhysRevB.109.174114.

(36) Adhikari, S.; Johari, P. Photovoltaic Properties of <math> <mrow> <mi>A</Mi> <mi>B</Mi> </Mrow> <msub> <mi Mathvariant="normal">Se</Mi> <mn>3</Mn> </Msub> </Math> Chalcogenide Perovskites (<math> <mi>A</Mi> </Math> = Ca, Sr, Ba; <math> <mi>B</Mi> </Math> = Zr, Hf). *Phys Rev B* **2024**, *109* (17), 174114. https://doi.org/10.1103/PhysRevB.109.174114.

(37) Kuhar, K.; Crovetto, A.; Pandey, M.; Thygesen, K. S.; Seger, B.; Vesborg, P. C. K.; Hansen, O.; Chorkendorff, I.; Jacobsen, K. W. Sulfide Perovskites for Solar Energy Conversion Applications: Computational Screening and Synthesis of the Selected Compound LaYS $_3$. *Energy Environ Sci* **2017**, *10* (12), 2579–2593. https://doi.org/10.1039/C7EE02702H.

(38) Sopiha, K. V.; Comparotto, C.; Márquez, J. A.; Scragg, J. J. S. Chalcogenide Perovskites: Tantalizing Prospects, Challenging Materials. *Adv Opt Mater* **2022**, *10* (3). https://doi.org/10.1002/adom.202101704.

(39) Wang, Y.; Lv, J.; Zhu, L.; Ma, Y. CALYPSO: A Method for Crystal Structure Prediction. *Comput Phys Commun* **2012**, *183* (10), 2063–2070. https://doi.org/10.1016/j.cpc.2012.05.008.

(40) Glass, C. W.; Oganov, A. R.; Hansen, N. USPEX—Evolutionary Crystal Structure Prediction. *Comput Phys Commun* **2006**, *175* (11–12), 713–720. https://doi.org/10.1016/j.cpc.2006.07.020.

(41) Wang, Y.; Baldassarri, B.; Shen, J.; He, J.; Wolverton, C. Landscape of Thermodynamic Stabilities of $A_2BB'O_6$ Compounds. *Chemistry of Materials* **2024**, *36* (14), 6816–6830. https://doi.org/10.1021/acs.chemmater.4c00576.

(42) Shahmohamadi, H.; Naghavi, S. S. Sulfide Perovskites for Thermoelectricity. *ACS Appl Mater Interfaces* **2021**, *13* (12), 14189–14197. https://doi.org/10.1021/acsami.0c22842.

(43) Li, W.; Wang, Z.; Deschler, F.; Gao, S.; Friend, R. H.; Cheetham, A. K. Chemically Diverse and Multifunctional Hybrid Organic–Inorganic Perovskites. *Nat Rev Mater* **2017**, *2* (3), 16099. https://doi.org/10.1038/natrevmats.2016.99.

(44) Bartel, C. J.; Sutton, C.; Goldsmith, B. R.; Ouyang, R.; Musgrave, C. B.; Ghiringhelli, L. M.; Scheffler, M. New Tolerance Factor to Predict the Stability of Perovskite Oxides and Halides. *Sci Adv* **2019**, *5* (2). https://doi.org/10.1126/sciadv.aav0693.

(45) Aykol, M.; Dwaraknath, S. S.; Sun, W.; Persson, K. A. Thermodynamic Limit for Synthesis of Metastable Inorganic Materials. *Sci Adv* **2018**, *4* (4). https://doi.org/10.1126/sciadv.aaq0148.

(46) Yao, Y.; Huang, Z.; Xie, P.; Lacey, S. D.; Jacob, R. J.; Xie, H.; Chen, F.; Nie, A.; Pu, T.; Rehwoldt, M.; Yu, D.; Zachariah, M. R.; Wang, C.; Shahbazian-Yassar, R.; Li, J.; Hu, L. Carbothermal Shock Synthesis of High-Entropy-Alloy Nanoparticles. *Science (1979)* **2018**, *359* (6383), 1489–1494. https://doi.org/10.1126/science.aan5412.

(47) Yao, Y.; Huang, Z.; Li, T.; Wang, H.; Liu, Y.; Stein, H. S.; Mao, Y.; Gao, J.; Jiao, M.; Dong, Q.; Dai, J.; Xie, P.; Xie, H.; Lacey, S. D.; Takeuchi, I.; Gregoire, J. M.; Jiang, R.; Wang, C.; Taylor, A. D.; Shahbazian-Yassar, R.; Hu, L. High-Throughput, Combinatorial Synthesis of Multimetallic Nanoclusters. *Proceedings of the National Academy of Sciences* **2020**, *117* (12), 6316–6322. https://doi.org/10.1073/pnas.1903721117.

(48) Jiang, K.; Siahrostami, S.; Zheng, T.; Hu, Y.; Hwang, S.; Stavitski, E.; Peng, Y.; Dynes, J.; Gangisetty, M.; Su, D.; Attenkofer, K.; Wang, H. Isolated Ni Single Atoms in Graphene Nanosheets for High-Performance CO_2 Reduction. *Energy Environ Sci* **2018**, *11* (4), 893–903. https://doi.org/10.1039/C7EE03245E.

(49) Du, Z.; Chen, X.; Hu, W.; Chuang, C.; Xie, S.; Hu, A.; Yan, W.; Kong, X.; Wu, X.; Ji, H.; Wan, L.-J. Cobalt in Nitrogen-Doped Graphene as Single-Atom Catalyst for High-Sulfur Content Lithium–Sulfur Batteries. *J Am Chem Soc* **2019**, *141* (9), 3977–3985. https://doi.org/10.1021/jacs.8b12973.

(50) Bartel, C. J.; Sutton, C.; Goldsmith, B. R.; Ouyang, R.; Musgrave, C. B.; Ghiringhelli, L. M.; Scheffler, M. New Tolerance Factor to Predict the Stability of Perovskite Oxides and Halides. *Sci Adv* **2019**, *5* (2). https://doi.org/10.1126/sciadv.aav0693.

(51) Schmidt, J.; Shi, J.; Borlido, P.; Chen, L.; Botti, S.; Marques, M. A. L. Predicting the Thermodynamic Stability of Solids Combining Density Functional Theory and Machine Learning. *Chemistry of Materials* **2017**, *29* (12), 5090–5103. https://doi.org/10.1021/acs.chemmater.7b00156.

(52) Jess, A.; Yang, R.; Hages, C. J. On the Phase Stability of Chalcogenide Perovskites. *Chemistry of Materials* **2022**, *34* (15), 6894–6901. https://doi.org/10.1021/acs.chemmater.2c01289.

(53) Friedman, J. H. Greedy Function Approximation: A Gradient Boosting Machine. *The Annals of Statistics* **2001**, *29* (5), 1189–1232.

(54) Ke, G.; Meng, Q.; Finley, T.; Chen, W.; Ye, Q.; Liu, T.-Y. LightGBM: A Highly Efficient Gradient Boosting Decision Tree. In *Advances in Neural Information Processing Systems*; 2017.

(55) Chen, T.; Guestrin, C. XGBoost. In *Proceedings of the 22nd ACM SIGKDD International Conference on Knowledge Discovery and Data Mining*; ACM: New York, NY, USA, 2016; pp 785–794. https://doi.org/10.1145/2939672.2939785.

(56) Ward, L.; Agrawal, A.; Choudhary, A.; Wolverton, C. A General-Purpose Machine Learning Framework for Predicting Properties of Inorganic Materials. *NPJ Comput Mater* **2016**, *2* (1), 16028. https://doi.org/10.1038/npjcompumats.2016.28.

(57) Bartel, C. J.; Trewartha, A.; Wang, Q.; Dunn, A.; Jain, A.; Ceder, G. A Critical Examination of Compound Stability Predictions from Machine-Learned Formation Energies. *NPJ Comput Mater* **2020**, *6* (1), 97. https://doi.org/10.1038/s41524-020-00362-y.

(58) Ward, L.; Liu, R.; Krishna, A.; Hegde, V. I.; Agrawal, A.; Choudhary, A.; Wolverton, C. Including Crystal Structure Attributes in Machine Learning Models of Formation Energies via Voronoi Tessellations. *Phys Rev B* **2017**, *96* (2), 024104. https://doi.org/10.1103/PhysRevB.96.024104.

(59) Kaundinya, P. R.; Choudhary, K.; Kalidindi, S. R. Machine Learning Approaches for Feature Engineering of the Crystal Structure: Application to the Prediction of the Formation Energy of Cubic Compounds. *Phys Rev Mater* **2021**, *5* (6), 063802. https://doi.org/10.1103/PhysRevMaterials.5.063802.

(60) Mao, Y.; Yang, H.; Sheng, Y.; Wang, J.; Ouyang, R.; Ye, C.; Yang, J.; Zhang, W. Prediction and Classification of Formation Energies of Binary Compounds by Machine Learning: An Approach without Crystal Structure Information. *ACS Omega* **2021**, *6* (22), 14533–14541. https://doi.org/10.1021/acsomega.1c01517.

(61) Tawfik, S. A.; Rashid, M.; Gupta, S.; Russo, S. P.; Walsh, T. R.; Venkatesh, S. Machine Learning-Based Discovery of Vibrationally Stable Materials. *NPJ Comput Mater* **2023**, *9* (1), 5. https://doi.org/10.1038/s41524-022-00943-z.

(62) Wang, Y.; Baldassarri, B.; Shen, J.; He, J.; Wolverton, C. Landscape of Thermodynamic Stabilities of $A_2BB'O_6$ Compounds. *Chemistry of Materials* **2024**, *36* (14), 6816–6830. https://doi.org/10.1021/acs.chemmater.4c00576.

(63) Tranchitella, L. J.; Chen, B.-H.; Fettinger, J. C.; Eichhorn, B. W. Structural Evolutions in the Sr1−Ba ZrSe3Series. *J Solid State Chem* **1997**, *130* (1), 20–27. https://doi.org/10.1006/jssc.1996.7253.

(64) Ju, M.; Dai, J.; Ma, L.; Zeng, X. C. Perovskite Chalcogenides with Optimal Bandgap and Desired Optical Absorption for Photovoltaic Devices. *Adv Energy Mater* **2017**, *7* (18). https://doi.org/10.1002/aenm.201700216.

(65) Shockley, W.; Queisser, H. J. Detailed Balance Limit of Efficiency of *p-n* Junction Solar Cells. *J Appl Phys* **1961**, *32* (3), 510–519. https://doi.org/10.1063/1.1736034.

(66) Rajan, A. C.; Mishra, A.; Satsangi, S.; Vaish, R.; Mizuseki, H.; Lee, K.-R.; Singh, A. K. Machine-Learning-Assisted Accurate Band Gap Predictions of Functionalized MXene. *Chemistry of Materials* **2018**, *30* (12), 4031–4038. https://doi.org/10.1021/acs.chemmater.8b00686.

(67) Zhuo, Y.; Mansouri Tehrani, A.; Brgoch, J. Predicting the Band Gaps of Inorganic Solids by Machine Learning. *J Phys Chem Lett* **2018**, *9* (7), 1668–1673. https://doi.org/10.1021/acs.jpclett.8b00124.

(68) Huang, Y.; Yu, C.; Chen, W.; Liu, Y.; Li, C.; Niu, C.; Wang, F.; Jia, Y. Band Gap and Band Alignment Prediction of Nitride-Based Semiconductors Using Machine Learning. *J Mater Chem C Mater* **2019**, *7* (11), 3238–3245. https://doi.org/10.1039/C8TC05554H.

(69) Gladkikh, V.; Kim, D. Y.; Hajibabaei, A.; Jana, A.; Myung, C. W.; Kim, K. S. Machine Learning for Predicting the Band Gaps of ABX $_3$ Perovskites from Elemental Properties. *The Journal of Physical Chemistry C* **2020**, *124* (16), 8905–8918. https://doi.org/10.1021/acs.jpcc.9b11768.

(70) Jain, A.; Ong, S. P.; Hautier, G.; Chen, W.; Richards, W. D.; Dacek, S.; Cholia, S.; Gunter, D.; Skinner, D.; Ceder, G.; Persson, K. A. Commentary: The Materials Project: A Materials Genome Approach to Accelerating Materials Innovation. *APL Mater* **2013**, *1* (1). https://doi.org/10.1063/1.4812323.

(71) Goodfellow, I. , B. Y. , & C. A. Deep Learning. *MIT Press* **2016**.

(72) Lee, J.; Seko, A.; Shitara, K.; Nakayama, K.; Tanaka, I. Prediction Model of Band Gap for Inorganic Compounds by Combination of Density Functional Theory Calculations and Machine Learning Techniques. *Phys Rev B* **2016**, *93* (11), 115104. https://doi.org/10.1103/PhysRevB.93.115104.

(73) Pilania, G.; Mannodi-Kanakkithodi, A.; Uberuaga, B. P.; Ramprasad, R.; Gubernatis, J. E.; Lookman, T. Machine Learning Bandgaps of Double Perovskites. *Sci Rep* **2016**, *6* (1), 19375. https://doi.org/10.1038/srep19375.

(74) Spearman, C. The Proof and Measurement of Association between Two Things. *Am J Psychol* **1904**, *15* (1), 72. https://doi.org/10.2307/1412159.

(75) Karl Pearson. III. Mathematical Contributions to the Theory of Evolution.—VIII. On the Inheritance of Characters Not Capable of Exact Quantitative Measurement.—Part I. Introductory. Part II. On the Inheritance of Coat-Colour in Horses. Part III. On the Inheritance of Eye-Colour in Man. *Philosophical Transactions of the Royal Society of London. Series A, Containing Papers of a Mathematical or Physical Character* **1901**, *195* (262–273), 79–150. https://doi.org/10.1098/rsta.1900.0024.

(76) Le Bahers, T.; Rérat, M.; Sautet, P. Semiconductors Used in Photovoltaic and Photocatalytic Devices: Assessing Fundamental Properties from DFT. *The Journal of Physical Chemistry C* **2014**, *118* (12), 5997–6008. https://doi.org/10.1021/jp409724c.

(77) Huang, B.; Deng, H.-X.; Lee, H.; Yoon, M.; Sumpter, B. G.; Liu, F.; Smith, S. C.; Wei, S.-H. Exceptional Optoelectronic Properties of Hydrogenated Bilayer Silicene. *Phys Rev X* **2014**, *4* (2), 021029. https://doi.org/10.1103/PhysRevX.4.021029.

(78) Kirchartz, T.; Rau, U. Linking Structural Properties with Functionality in Solar Cell Materials – the Effective Mass and Effective Density of States. *Sustain Energy Fuels* **2018**, *2* (7), 1550–1560. https://doi.org/10.1039/C7SE00622E.

(79) Du, M. H. Efficient Carrier Transport in Halide Perovskites: Theoretical Perspectives. *J Mater Chem A Mater* **2014**, *2* (24), 9091–9098. https://doi.org/10.1039/C4TA01198H.

(80) Yu, L.; Zunger, A. Identification of Potential Photovoltaic Absorbers Based on First-Principles Spectroscopic Screening of Materials. *Phys Rev Lett* **2012**, *108* (6), 068701. https://doi.org/10.1103/PhysRevLett.108.068701.

(81) Cai, Y.; Xie, W.; Teng, Y. T.; Harikesh, P. C.; Ghosh, B.; Huck, P.; Persson, K. A.; Mathews, N.; Mhaisalkar, S. G.; Sherburne, M.; Asta, M. High-Throughput Computational Study of Halide Double Perovskite Inorganic Compounds. *Chemistry of Materials* **2019**, *31* (15), 5392–5401. https://doi.org/10.1021/acs.chemmater.9b00116.

(82) Yang, J.; Manganaris, P.; Mannodi-Kanakkithodi, A. A High-Throughput Computational Dataset of Halide Perovskite Alloys. *Digital Discovery* **2023**, *2* (3), 856–870. https://doi.org/10.1039/D3DD00015J.

(83) Schileo, G.; Grancini, G. Lead or No Lead? Availability, Toxicity, Sustainability and Environmental Impact of Lead-Free Perovskite Solar Cells. *J Mater Chem C Mater* **2021**, *9* (1), 67–76. https://doi.org/10.1039/D0TC04552G.

(84) Yuan, Z.; Dahliah, D.; Claes, R.; Pike, A.; Fenning, D. P.; Rignanese, G.-M.; Hautier, G. Assessing Carrier Mobility, Dopability, and Defect Tolerance in the Chalcogenide Perovskite <math Display="inline" Overflow="scroll"> <msub> <mrow> <mi>Ba</Mi> <mi>Zr</Mi> <mi Mathvariant="normal">S</Mi> </Mrow> <mn>3</Mn> </Msub> </Math>. *PRX Energy* **2024**, *3* (3), 033008. https://doi.org/10.1103/PRXEnergy.3.033008.

(85) Lelieveld, R.; IJdo, D. J. W. Sulphides with the GdFeO $_3$ Structure. *Acta Crystallogr B* **1980**, *36* (10), 2223–2226. https://doi.org/10.1107/S056774088000845X.

(86) Whitehead, R. C.; VanSant, K. T.; Warren, E. L.; Buencuerpo, J.; Rienäcker, M.; Peibst, R.; Geisz, J. F.; Tamboli, A. C. Optimization of Four Terminal Rear Heterojunction GaAs on Si Interdigitated Back Contact Tandem Solar Cells. *Appl Phys Lett* **2021**, *118* (18), 183902. https://doi.org/10.1063/5.0049097/13109107/183902_1_ACCEPTED_MANUSCRIPT.PDF.

(87) Looker, Q.; Wood, M. G.; Lake, P. W.; Kim, J. K.; Serkland, D. K. GaAs X-Ray Detectors with Sub-Nanosecond Temporal Response. *Review of Scientific Instruments* **2019**, *90* (11). https://doi.org/10.1063/1.5127294.

(88) Prezhdo, O. V. Photoinduced Dynamics in Semiconductor Quantum Dots: Insights from Time-Domain *Ab Initio* Studies. *Acc Chem Res* **2009**, *42* (12), 2005–2016. https://doi.org/10.1021/ar900157s.

(89) Li, W.; Vasenko, A. S.; Tang, J.; Prezhdo, O. V. Anharmonicity Extends Carrier Lifetimes in Lead Halide Perovskites at Elevated Temperatures. *Journal of Physical Chemistry Letters* **2019**, *10* (20), 6219–6226. https://doi.org/10.1021/ACS.JPCLETT.9B02553/ASSET/IMAGES/LARGE/JZ9B02553_0006.JPEG.

(90) Walker, A. W.; Heckelmann, S.; Karcher, C.; Höhn, O.; Went, C.; Niemeyer, M.; Bett, A. W.; Lackner, D. Nonradiative Lifetime Extraction Using Power-Dependent Relative Photoluminescence of III-V Semiconductor Double-Heterostructures. *J Appl Phys* **2016**, *119* (15). https://doi.org/10.1063/1.4945772.

(91) Long, R.; Prezhdo, O. V. Quantum Coherence Facilitates Efficient Charge Separation at a MoS_2 /$MoSe_2$ van Der Waals Junction. *Nano Lett* **2016**, *16* (3), 1996–2003. https://doi.org/10.1021/acs.nanolett.5b05264.

(92) Long, R.; Liu, J.; Prezhdo, O. V. Unravelling the Effects of Grain Boundary and Chemical Doping on Electron–Hole Recombination in $CH_3NH_3PbI_3$ Perovskite by Time-Domain Atomistic Simulation. *J Am Chem Soc* **2016**, *138* (11), 3884–3890. https://doi.org/10.1021/jacs.6b00645.

(93) Gross, N.; Sun, Y.-Y.; Perera, S.; Hui, H.; Wei, X.; Zhang, S.; Zeng, H.; Weinstein, B. A. Stability and Band-Gap Tuning of the Chalcogenide Perovskite <math Display="inline"> <mrow> <msub> <mrow> <mi>BaZrS</Mi> </Mrow> <mrow> <mn>3</Mn> </Mrow> </Msub> </Mrow> </Math> in Raman and Optical Investigations at High Pressures. *Phys Rev Appl* **2017**, *8* (4), 044014. https://doi.org/10.1103/PhysRevApplied.8.044014.

(94) Singh, S.; Nayak, P. K.; Tretiak, S.; Ghosh, D. Composition Dependent Strain Engineering of Lead-Free Halide Double Perovskite: Computational Insights. *J Phys Chem Lett* **2023**, *14* (42), 9479–9489. https://doi.org/10.1021/acs.jpclett.3c02249.

(95) Hanzawa, K.; Iimura, S.; Hiramatsu, H.; Hosono, H. Material Design of Green-Light-Emitting Semiconductors: Perovskite-Type Sulfide $SrHfS_3$. *J Am Chem Soc* **2019**, *141* (13), 5343–5349. https://doi.org/10.1021/jacs.8b13622.

(96) Yasmin, N.; Safdar, M.; Ali, G.; Khan, H. M.; Mirza, M. Solar Light Harvesting Nanomaterial (BaZrS3) for Photocatalytic Activity and OER Reaction. *Journal of Physics and Chemistry of Solids* **2023**, *172*, 111056. https://doi.org/10.1016/j.jpcs.2022.111056.

(97) Cao, Y.; Dai, S.; Wang, X.; Wei, T.; Yang, J.; Xi, L.; Pang, Z.; Tan, G. High-Throughput Screening of Potentially Ductile and Low Thermal Conductivity ABX3 (X = S, Se, Te) Thermoelectric Perovskites. *Appl Phys Lett* **2024**, *124* (9). https://doi.org/10.1063/5.0188454.

(98) Kresse, G.; Hafner, J. *Ab Initio* Molecular Dynamics for Liquid Metals. *Phys Rev B* **1993**, *47* (1), 558–561. https://doi.org/10.1103/PhysRevB.47.558.

(99) Kresse, G.; Hafner, J. *Ab Initio* Molecular-Dynamics Simulation of the Liquid-Metal–Amorphous-Semiconductor Transition in Germanium. *Phys Rev B* **1994**, *49* (20), 14251–14269. https://doi.org/10.1103/PhysRevB.49.14251.

(100) Perdew, J. P.; Burke, K.; Ernzerhof, M. Generalized Gradient Approximation Made Simple. *Phys Rev Lett* **1996**, *77* (18), 3865–3868. https://doi.org/10.1103/PhysRevLett.77.3865.

(101) Steiner, S.; Khmelevskyi, S.; Marsmann, M.; Kresse, G. Calculation of the Magnetic Anisotropy with Projected-Augmented-Wave Methodology and the Case Study of Disordered <math> <mrow> <msub> <mi>Fe</Mi> <mrow> <mn>1</Mn> <mo>−</Mo> <mi>x</Mi> </Mrow> </Msub> <msub> <mi>Co</Mi> <mi>x</Mi> </Msub> </Mrow> </Math> Alloys. *Phys Rev B* **2016**, *93* (22), 224425. https://doi.org/10.1103/PhysRevB.93.224425.

(102) Kresse, G.; Joubert, D. From Ultrasoft Pseudopotentials to the Projector Augmented-Wave Method. *Phys Rev B* **1999**, *59* (3), 1758–1775. https://doi.org/10.1103/PhysRevB.59.1758.

(103) Heyd, J.; Scuseria, G. E.; Ernzerhof, M. Hybrid Functionals Based on a Screened Coulomb Potential. *J Chem Phys* **2003**, *118* (18), 8207–8215. https://doi.org/10.1063/1.1564060.

(104) Krukau, A. V.; Vydrov, O. A.; Izmaylov, A. F.; Scuseria, G. E. Influence of the Exchange Screening Parameter on the Performance of Screened Hybrid Functionals. *J Chem Phys* **2006**, *125* (22). https://doi.org/10.1063/1.2404663.

(105) Kirklin, S.; Saal, J. E.; Meredig, B.; Thompson, A.; Doak, J. W.; Aykol, M.; Rühl, S.; Wolverton, C. The Open Quantum Materials Database (OQMD): Assessing the Accuracy of DFT Formation Energies. *NPJ Comput Mater* **2015**, *1* (1), 15010. https://doi.org/10.1038/npjcompumats.2015.10.

(106) Li, W.; Walther, C. F. J.; Kuc, A.; Heine, T. Density Functional Theory and Beyond for Band-Gap Screening: Performance for Transition-Metal Oxides and Dichalcogenides. *J Chem Theory Comput* **2013**, *9* (7), 2950–2958. https://doi.org/10.1021/ct400235w.

(107) Ward, L.; Agrawal, A.; Choudhary, A.; Wolverton, C. A General-Purpose Machine Learning Framework for Predicting Properties of Inorganic Materials. *NPJ Comput Mater* **2016**, *2* (1), 16028. https://doi.org/10.1038/npjcompumats.2016.28.

(108) Guyon, I.; Weston, J.; Barnhill, S.; Vapnik, V. Gene Selection for Cancer Classification Using Support Vector Machines. *Mach Learn* **2002**, *46* (1/3), 389–422. https://doi.org/10.1023/A:1012487302797.

The data supporting this article have been included as part of the Supplementary Information.